Deep structure of the Baringo Rift Basin (central Kenya) from three-dimensional magnetotelluric imaging: Implications for rift evolution

JOURNAL OF GEOPHYSICAL RESEARCH, VOL. 105, NO. B10, PAGES 23,493–23,518, OCTOBER 10, 2000

Deep structure of the Baringo Rift Basin (central Kenya) from three-dimensional magnetotelluric imaging: Implications for rift evolution

Sophie Hautot and Pascal Tarits

UMR CNRS 6538 "Domaines Océaniques", IUEM/UBO, Plouzané, France

Kathy Whaler

Grant Institute, Department of Geology and Geophysics, University of Edinburgh, Edinburgh, Scotland, United Kingdom

Bernard Le Gall, Jean-Jacques Tiercelin, and Caroline Le Turdu

UMR CNRS 6538 "Domaines Océaniques", IUEM/UBO, Plouzané, France

Abstract. Three-dimensional modeling of data from 31 vertical electrical and 24 magnetotelluric soundings collected in the Baringo-Bogoria Basin (central Kenya Rift Valley) shows a thick succession of well-defined tectonostratigraphic units beneath the Recent deposits of the Marigat-Loboi Plain. They include from top to bottom, a sedimentary basin, ~1.5 km thick, controlled by N-S and N140° structural trends, and a thick homogeneous resistive layer related to the bottom of the basin, overlying a conductive structure, which cannot be clearly correlated with the Proterozoic basement. It is suggested that the resistive layer correlates with the mid-Miocene plateau-type flood phonolites which flowed over the early Kenya Rift during a major volcanic activity period. The conductive structure overlain by these lava flows could be a sedimentary basin developed during the initial phase of rifting, during the Oligocene-Miocene. The absence of a significant gravity low associated with this deep basin suggests a zone of dense intrusion deeper than 5-10 km, not discernible with the magnetotelluric data but required to explain the gravity anomalies. The recognition of a deeply buried sedimentary succession lying between 4 and 8 km beneath the lower Miocene volcanic series of the Baringo valley would provide new insights into the regional volcano-sedimentary stratigraphic succession and the rift development of the Kerio and Baringo Basins.

1. Introduction

The Kenya Rift is part of the eastern branch of the East African Rift System. It consists of a linear structure that extends over ~900 km from the Turkana Basin at 4°30'N to the North Tanzanian Divergence (NTD) at 2°S (Figure 1a). Between the equator and 1°N, the central Kenya Rift is a 100-km-wide, strongly asymmetric graben structure with a double western margin delineated by the Elgeyo and Saimo/Kito Pass boundary faults, the latter delineating the Tugen Hills horst. Its eastern flank is marked by a series of en échelon fault-scarps forming the Laikipia Rift Border Fault [*Chapman et al.*, 1978; *Williams and Chapman*, 1986] (Figures 1b and 2). East of the Saimo Fault, the 50-km-long, 20-km-wide Baringo-Bogoria Basin (BBB), presently occupied by the freshwater Lake Baringo to the north and the soda Lake Bogoria to the south, has been described as a classic easterly tilted half graben [*Tiercelin et al.*, 1980] and considered as part of the present-day active axial valley of the Kenya Rift [*Chapman et al.*, 1978; *Tiercelin and Vincens*, 1987; *Le Turdu et al.*, 1995].

The subsurface structure of the central and northern Kenya Rift has been documented by industrial reflection seismic and gravity data, demonstrating that extensional processes initiated during Paleogene time with the development of complex half grabens up to 7 km deep (the Kerio and Lokichar half grabens) [*Morley et al.*, 1992; *Smith and Mosley*, 1993; *Mugisha et al.*, 1997] (Figure 1a), in an area of great lithospheric complexity related to Late Proterozoic orogenic events [*McConnell*, 1972; *King*, 1978]. Several regional seismic and gravity models have been proposed for the deep crust and mantle structure of the Kenya Rift; of particular inter-

Paper number 2000JB900213.
0148-0227/00/2000JB900213$09.00

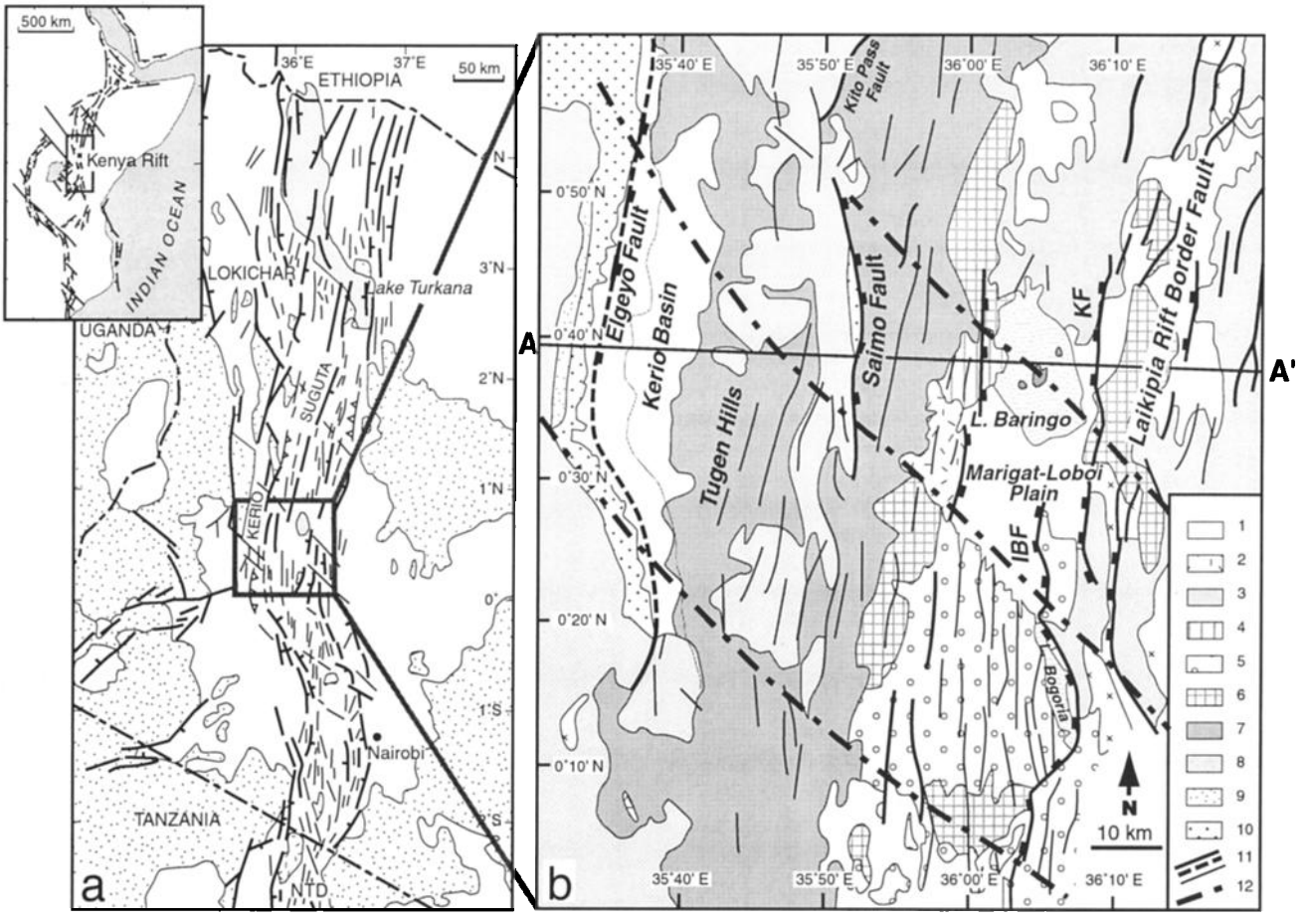

Figure 1. (a) Location map of the Kenya Rift. Modified from *Dunkley et al.* [1993]. NTD, North Tanzanian Divergence. (b) Simplified geological map of the Kerio-Baringo Basins. 1, undifferentiated Pleistocene rocks; 2, Kapthurin Formation; 3, Karosi volcanics; 4, Baringo volcanics; 5, Hannington Trachyphonolites; 6, undifferentiated Pleistocene volcanics; 7, undifferentiated Pliocene rocks; 8, undifferentiated Miocene rocks; 9, Tambach Formation; 10, Precambrian basement; 11, faults; 12, transverse faults, Late Proterozoic shear zones. KF, Karau Fault; IBF, Ilosowuani-Bechot Fault.

est here are those in the Baringo region [*KRISP Working Party,* 1991; *Swain,* 1992; *Achauer and the KRISP Teleseismic Working Group,* 1994; *Swain et al.,* 1994; *Hay et al.,* 1995].

Recent structural field work and remote sensing studies have provided new information on the structure of the BBB, with several structural blocks having been identified [*Le Turdu,* 1998] (Figure 3). Among them, the east dipping, N-S trending Bogoria block corresponds to a "giant grid fault" basin [*Le Turdu et al.,* 1995]. North of Bogoria, the Baringo-Marigat-Loboi block corresponds to a 30-km-long and 20-km-wide rhomb-shaped structure occupied by the Marigat-Loboi alluvial plain and the southern end of Lake Baringo. This structure is bounded to the north and south by N140-150° trending lineaments (POKTZ and WMTZ, Figures 1b and 3) which are clearly visible on SPOT imagery [*Le Turdu et al.,* 1995; *Le Turdu,* 1998] and identified from gravity and aeromagnetic data as deep basement-controlled features [*Smith and Mosley,* 1993]. The importance of such deep basement structures during the evolution of the Kenya Rift has been clearly demonstrated by various authors [e.g., *McConnell,* 1972; *King,* 1978; *Smith and Mosley,* 1993]. In particular, NW trending basement structures corresponding to ductile-brittle shear zones active into the Late Proterozoic control the location of large transfer zones that segment the rift into several rhomb-shaped blocks (Figure 3), as well as the distribution of large axial volcanoes to the south and north of the BBB [*Dunkley et al.,* 1993; *Le Turdu et al.,* 1995]. Earlier magnetotelluric, seismic, and gravity surveys suggested a 0.5 to 1 km sediment thickness below the surface of the Marigat-Loboi Plain [*Rooney and Hutton,* 1977; *Swain et al.,* 1981]. On the basis of these geophysical results and structural field observations, the Marigat-Loboi Plain was interpreted as a typical "pull-apart" basin [*Richert et al.,* 1987].

In order to further investigate the deep structure of the BBB, we carried out a detailed geophysical survey by means of vertical electric sounding (VES) and mag-

netotelluric (MT) methods. Thirty-one VES soundings and twenty-four MT soundings were collected over the BBB, allowing us to obtain a full three-dimensional (3-D) geoelectrical model of the basin down to ~10 km. The interpretation of the MT data set provided some new insights that led us (1) to apply a new lithostratigraphic rift succession to the Baringo axial basin, (2) to establish lateral correlation with the nearby Kerio half graben to the west, and (3) to discuss the mode of rift propagation across the central Kenya rifted zone.

Section 2 provides a review of the regional stratigraphy and evolution of the central Kenya Rift (between the equator and 1°N). In section 3 we present the geophysical data collection and processing. The 3-D MT modeling is detailed, followed by a sensitivity analysis of our preferred model. Finally, in sections 4, 5 and 6 we discuss the implications of the model for the geological understanding of the area.

2. Stratigraphic Outline and Evolution of the Central Kenya Rift

The general evolutionary history of the central Kenya Rift is quite well documented by the interbedded volcanic and sedimentary formations that outcrop above Precambrian basement rocks along the Elgeyo and Saimo/Kito Pass Faults escarpments to the west and along the Laikipia Rift Border Fault to the east [*Chapman et al.*, 1978; *Andrews and Banham*, 1999]. Detailed stratigraphies are presented in Figures 1b and 2.

2.1. From Paleogene to Mid-Miocene

Rifting began during Paleogene time in the west of the central Kenya Rift and to the north with the formation of the fault-bounded Kerio and Lokichar Basins [*Morley et al.*, 1992; *Mugisha et al.*, 1997]. Contemporary sedimentary formations (Kimwarer to the west; Kamego to the east) rest on the Precambrian basement (Figure 2). This first phase of rifting is also marked by intense volcanic activity that largely transgresses the limits of the initial rifted zone. It is represented in the central Kenya Rift by the 900-m-thick Elgeyo Basalts and Chof Phonolites on the western side, the 800- to 1200-m-thick Sidekh Phonolite Formation in the central part, and the 1000-m-thick Samburu Basalts to the east (Figure 2). During this period, the ~400-m-thick Tambach fluvio-lacustrine formation was also deposited. It overlies the Precambrian basement north of 0°30'N and

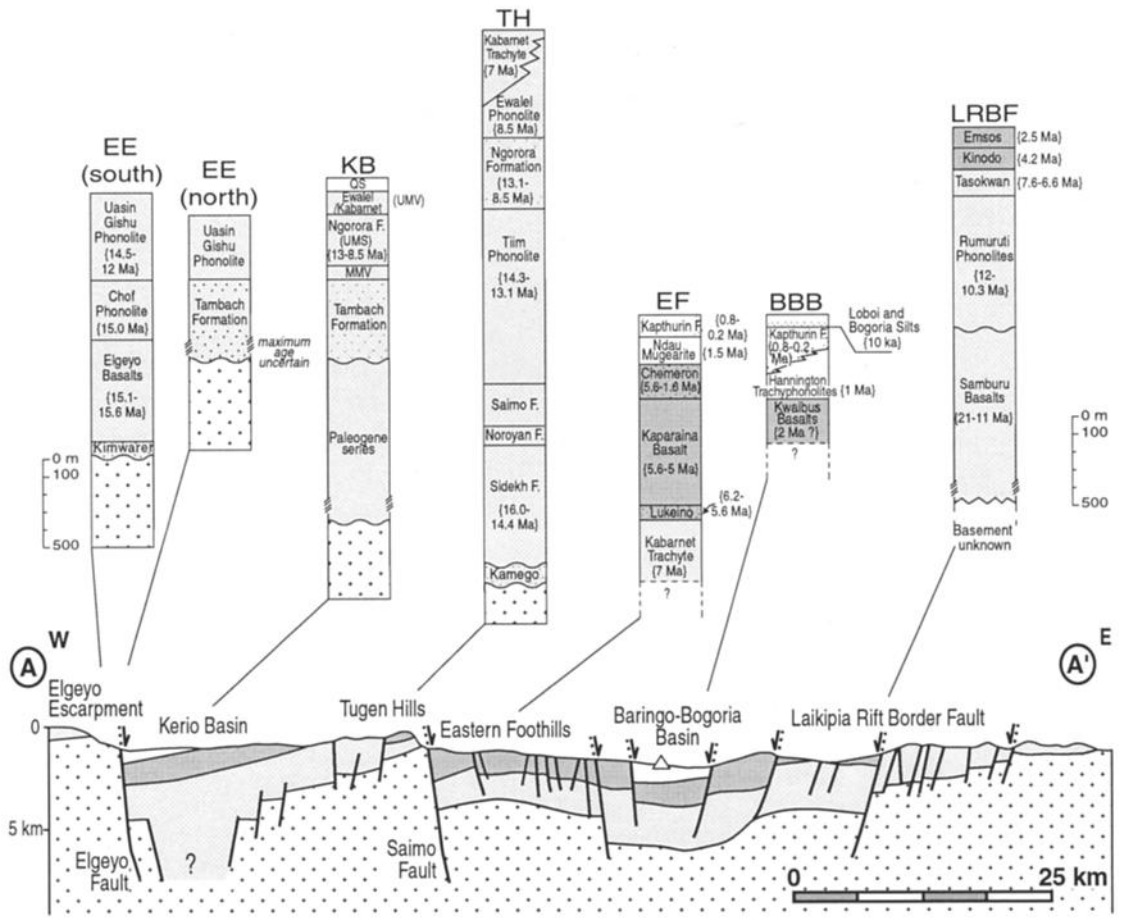

Figure 2. (top) Stratigraphic series from the Elgeyo Fault to the west to the Laikipia escarpment to the east. (bottom) Simplified cross section of the stratigraphic series. Same legend as for Figure 1b. UMV, upper Miocene volcanics; UMS, upper Miocene sediments; MMV, mid-Miocene volcanics.

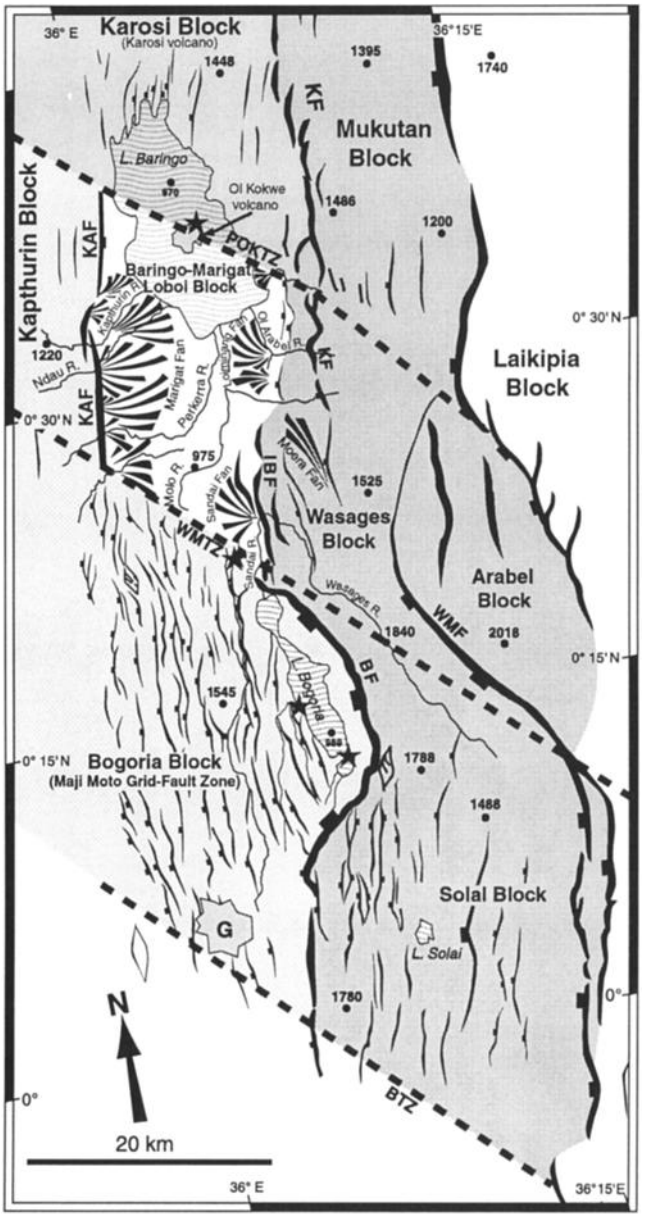

Figure 3. Structural map of the central Kenya Rift valley between 0° and 0°50'N. The location of the major faults is shown (WMF, Wasages-Marmanet Fault; BF, Bogoria Fault; KAF, Kapthurin Fault; KF, Karau Fault; IBF, Ilosowuani-Bechot Fault; POKTZ, Porumbonyanza-Ol Kokwe Transverse Zone; WMTZ, Wasages-Marmanet Transverse Zone; BTZ, Bahati Transverse Zone). Stars indicate hydrothermal activity.

has been interpreted as filling a shallow sag basin [*Chapman et al.*, 1978; *Morley et al.*, 1992; *Mugisha et al.*, 1997; *Renaut et al.*, 1999].

This Paleogene to mid-Miocene phase of rifting ended with the deposition of flood phonolites that overflowed both rift shoulders, with the 500- to >1000-m-thick Uasin Gishu Phonolites on the Elgeyo escarpment, the Tiim Phonolites on the Saimo Fault escarpment, and the Rumuruti Phonolites to the east [*Lippard*, 1972; *Griffiths*, 1977; *Chapman et al.*, 1978; *Chapman and Brook*, 1978; *Deino et al.*, 1990] (Figure 2).

2.2. From Mid-Miocene to Upper Miocene

A second episode of rifting defined by *Mugisha et al.* [1997] is marked by (1) considerable fault displacement along the Elgeyo Fault, the western rift boundary, and (2) the deposition of the 400-m-thick fluvio-lacustrine Ngorora Formation within a tectonically active half graben [*Chapman et al.*, 1978; *Hill*, 1999]. Subsequent volcanic activity in this area resulted in the deposition of the Ewalel Phonolites, followed by the eruption of the Kabarnet Trachytes [*Chapman et al.*, 1978]. On the eastern border of the rift, the Tasokwan Trachytes were deposited by similar trachytic eruptions (Figure 2). Tectonic activity preceding these trachytes eruptions resulted in the formation of the eastern most of the Laikipia Fault escarpments and uplift along the Saimo Fault [*Griffiths*, 1977; *Chapman et al.*, 1978].

2.3. From Lower Pliocene to Present

Several authors [*Tiercelin*, 1981; *Bosworth*, 1985; *Morley*, 1994] proposed that from lower Pliocene to the Present, tectonism, volcanism, and sedimentation migrated eastward from the western Elgeyo Fault into a narrow zone corresponding to the present-day axis of the rift. At 5.6 Ma, the Kaparaina Basalts were deposited by fissure-style eruptions on the western side of this inner trough, corresponding to the immediate hanging wall of the Saimo Fault [*Chapman and Brook*, 1978; *Hill*, 1999] (Figure 2). Then these basalts were deformed by major tectonic movements [*Chapman et al.*, 1978], while lake basins developed on the hanging wall of the Saimo Fault [*Bishop*, 1971; *Pickford*, 1975; *Hill*, 1999]. Major faulting and uplift occurred along the Saimo Fault and resulted in the full development of the active axis of the Kenya Rift to the east [*Baker et al.*, 1972; *Tiercelin*, 1981; *Tiercelin et al.*, 1981; *Bosworth*, 1985; *Morley*, 1994] corresponding to the BBB between the equator and 1°N.

Intense volcanic activity resulted in the deposition of numerous, young volcanic products such as the Hannington Trachyphonolites [*Griffiths and Gibson*, 1980], mainly on the western side of the BBB, and in the development of the Karosi axial volcano at the northern end of the basin (Figure 3). Contemporaneous tectonic movements and erosion along the Saimo Fault escarpment caused in the accumulation in the axial trough of the 125-m-thick Kapthurin fluvio-lacustrine formation (KFm).

2.4. Present-Day Structure of the Baringo-Bogoria Basin

The BBB structure is complex and controlled by N0-10° and N140-150° basement- inherited tectonic trends, with minor influence of a N50° trend at the southern end of Lake Bogoria (Figure 3). The northern two thirds of the BBB comprise (from the south) the Marigat-Loboi alluvial plain and Lake Baringo Basin, which together form a 50-km-long, 20-km-wide rhomb-shaped

structure, with the Baringo Basin closed at its northern end by the Karosi volcano (Figure 3).

The westernmost limit of the BBB corresponds to the Saimo Fault, with an immediate western border corresponding to the N-S trending Kapthurin Fault (KAF) (Figure 3), which cuts the KFm and contemporaneous lavas [*Le Gall et al.*, 2000]. The southwestern edge of the BBB corresponds to the Maji Moto grid fault zone formed by kilometer-long, 10- to 100-m throw, anastomosed faults which intensely slice the Hannington Trachyphonolites Formation [*Tiercelin et al.*, 1981; *Grimaud et al.*, 1994] (Figure 3). The resulting N-S trending, easterly tilted blocks dip gently to the north beneath the Marigat-Loboi Plain sediments, the contact following a N150° trend [*Le Turdu et al.*, 1995].

To the east, the BBB is bounded by a complex strip of N-S trending, westward dipping, en échelon synthetic and antithetic step faults of the Laikipia Fault, some with vertical displacements exceeding 1000-1500 m in places [*Le Turdu et al.*, 1995]. The immediate eastern border of the BBB corresponds to the Karau Fault (KF) that affects the Hannington and Karau volcanics (Figures 1b and 3).

To the south, the 600-m apparent throw, N-S trending Bogoria Fault (BF) forms the eastern border of the Bogoria Basin. At the southeastern corner of the Marigat-Loboi Plain, the N-S tectonic trend expressed in the median segment of the BF is represented by a series of kilometer-long, east dipping structural blocks, the Ilosowuani-Bechot horst bounded to the east by the Ilosowuani-Bechot Fault (IBF), affecting the Hannington lavas (Figure 3). At its northern tip, the BF gently curves toward N150° and coincides with the northeastern boundary of the Maji Moto grid fault system.

The particular rhomb-shaped morphology of the Marigat-Loboi Plain is directly linked to the N140° trending structures identified by geophysical methods in the central and northern Kenya Rift as Precambrian ductile-brittle shear zones [*Dunkley et al.*, 1993; *Smith and Mosley*, 1993] (Figures 1b and 3). The Porumbonyanza-Ol Kokwe Transverse Zone (POKTZ) defined by *Le Turdu et al.* [1995] (also named the Ol Arabel Fault Zone (OBFZ) by Smith and *Mosley* [1993]) forms the northern boundary of the Marigat-Loboi Plain. Its southern limit corresponds to the Wasages-Marmanet Transverse Zone (WMTZ), which is clearly expressed at the surface by the marked cartographic curvature of both the Wasages-Marmanet Fault (WMF) and the BF, as well as by the flexuring to the north of the Maji-Moto grid fault zone beneath the Marigat-Loboi Plain.

The Recent to present-day sedimentation in the BBB is essentially of detrital origin. The major sedimentary bodies belong to three different types, alluvial fans, river channel systems, and lake bodies (Figure 4). All are linked to a complex perennial or semiperennial hydrographic network and are mainly controlled by N-S and N140° structural trends (Figure 3). Alluvial fans develop along the faulted margins of the BBB. The central and northeastern parts of the Marigat-Loboi consist of complex channel systems, and up to 20 m of fluvial to lacustrine holocene age silts (Loboi and Borgoria silts) crop out over a large area of the plain. Freshwater and saline lake environments characterize the northern and southern ends of the basin, respectively, as well as strong hydrothermal activity mainly located in the Bogoria block [*Tiercelin et al.*, 1980; *Renaut*, 1982; *Tiercelin and Vincens*, 1987] (Figure 3).

3. Experiment and Data Processing

3.1. Vertical Electric Soundings

Thirty-one vertical electric resistivity soundings (VES) were collected in the Marigat- Loboi Plain in the BBB, using the Schlumberger array electrode configuration (Figure 4). The maximum current electrode half spacing (AB/2) was 300 m. Typically, the apparent resistivity is <100 Ω m near the surface. It decreases down to very low values, <2 Ω m (Figure 5a), and, for some sites, increases at the largest electrode spacing (Figure 5b).

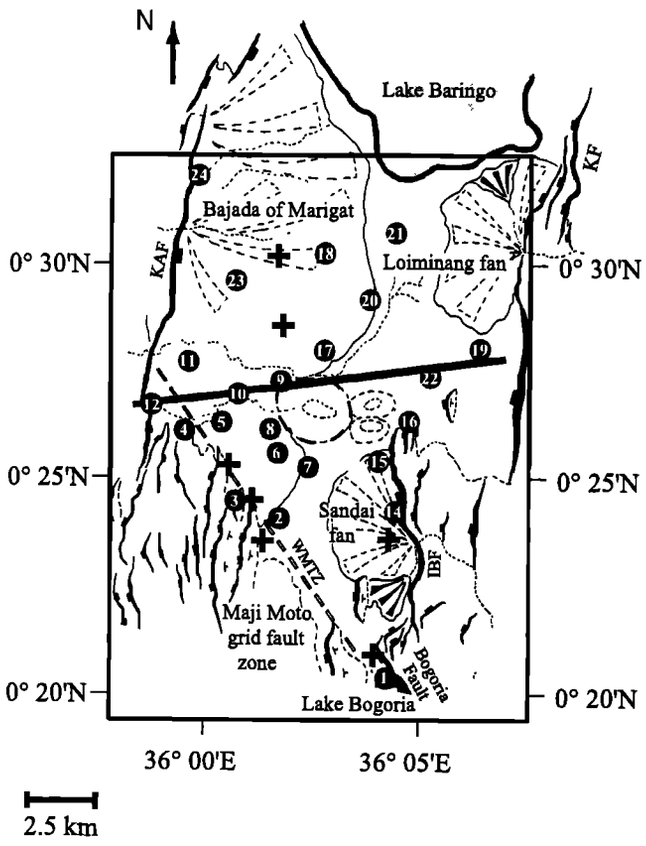

Figure 4. Structural map of the Marigat-Loboi Plain, synthesized from remote-sensing analysis and field observations. The locations of the MT and VES sites (solid circles) and of the seven additional VES sites (crosses) are shown. The surface area of the 3-D model is enclosed by a box. The heavy line is the profile used for the 2-D preliminary inversion. WMTZ, Wasages-Marmanet Transverse Zone; KF, Karau Fault; IBF, Ilosowuani-Bechot Fault; KAF, Kapthurin Fault.

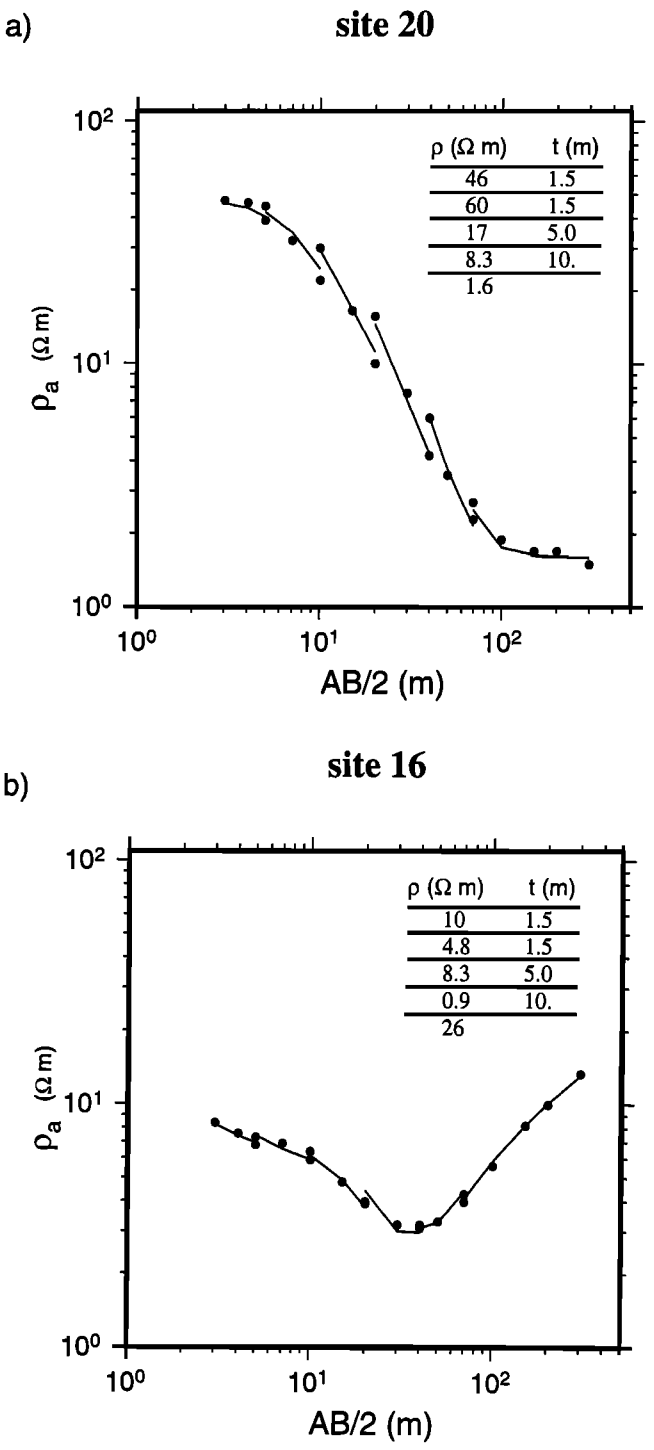

Figure 5. Vertical electrical soundings: apparent resistivity curves at sites (a) 20 and (b) 16. The 1-D inversion contains differing potential electrode spacings. Dots indicate the measured data; solid lines indicate the response of the 1-D model. The resistivities (ρ) and thicknesses (t) of the four-layer model are given in the top right.

The apparent resistivity data at each site were modeled with a one-dimensional four-layer resistivity structure overlying a homogeneous half-space. The thickness of each layer is fixed (1.5, 1.5, 5, and 10 m) and is identical at each site. The number of layers and their thicknesses were chosen to provide a solution at all sites. A nonlinear steepest gradient method was used to determine the resistivity section at each site. The objective function minimized was the squared misfit between the data and the model responses, regularized by the addition of the sum of the squared differences of log(resistivity) between two adjacent layers multiplied by a damping parameter. The regularization ensured that spurious models were not obtained when data suggested less than four layers. The model responses fit the data well at all sites, as illustrated by the two examples (sites 16 and 20) in Figure 5.

3.2. Magnetotelluric (MT) Soundings

3.2.1. Data processing. We carried out 24 MT soundings at a subset of the VES sites (Figure 4) with the Short Period Automatic Magnetotelluric (SPAM) Mark III data acquisition system [*Ritter et al.*, 1998] with induction coils (ECA CM11E). The horizontal electric and magnetic field time series were recorded in seven independent period bands (band 0, 0.0078125-0.0625 s; band 1, 0.0625-0.25 s; band 2, 0.25-1 s; band 3, 1-4 s; band 4, 4-16 s; band 5, 16-64 s; and band 6, 64-256 s) in the magnetic north, x, and east, y, directions. The electric potentials were measured between two nonpolarizable Cl_2-$PbCl_2$ electrodes, with a separation of 50 m. The recordings typically lasted 6 to 10 hours, some during the day and others overnight. The station spacing was roughly 2-3 km, depending on accessibility in the field (Figure 4). The position of each station was obtained with a portable GPS unit.

For each period band the electric and magnetic field time series were transformed into the frequency domain. The 2x2 magnetotelluric (MT) impedance tensor Z relating the horizontal electric (E_x, E_y) to the horizontal magnetic fields (B_x, B_y) was determined using the robust remote reference method of *Chave and Thomson* [1989].

The data in the three shortest-period bands (0, 1, and 2) are of excellent quality, leading to a very precise MT impedance. The data in the longer-period bands (3 to 6) did not provide such good transfer functions because of the limited recording time and the lack of electromagnetic energy in the period range 1-10 s, known as the dead band (bands 3 and 4). The longest reliable period common to all sites is 85.3 s, but either period 128 s or 170 s or both are available at most of the sites. Examples of transfer functions at four sites (3, 9, 22, and 23) are presented in Figure 6. Both the amplitudes and phases of the off-diagonal terms (xy and yx) and the amplitudes of the diagonal terms (xx and yy) are shown. The amplitudes are expressed in apparent resistivity units (Ω m), and the error bars are one standard deviation. These four sites represent a fair sampling of the variability of the MT impedance across the BBB. They also illustrate the variation of data quality with period. In the dead band we had to remove several

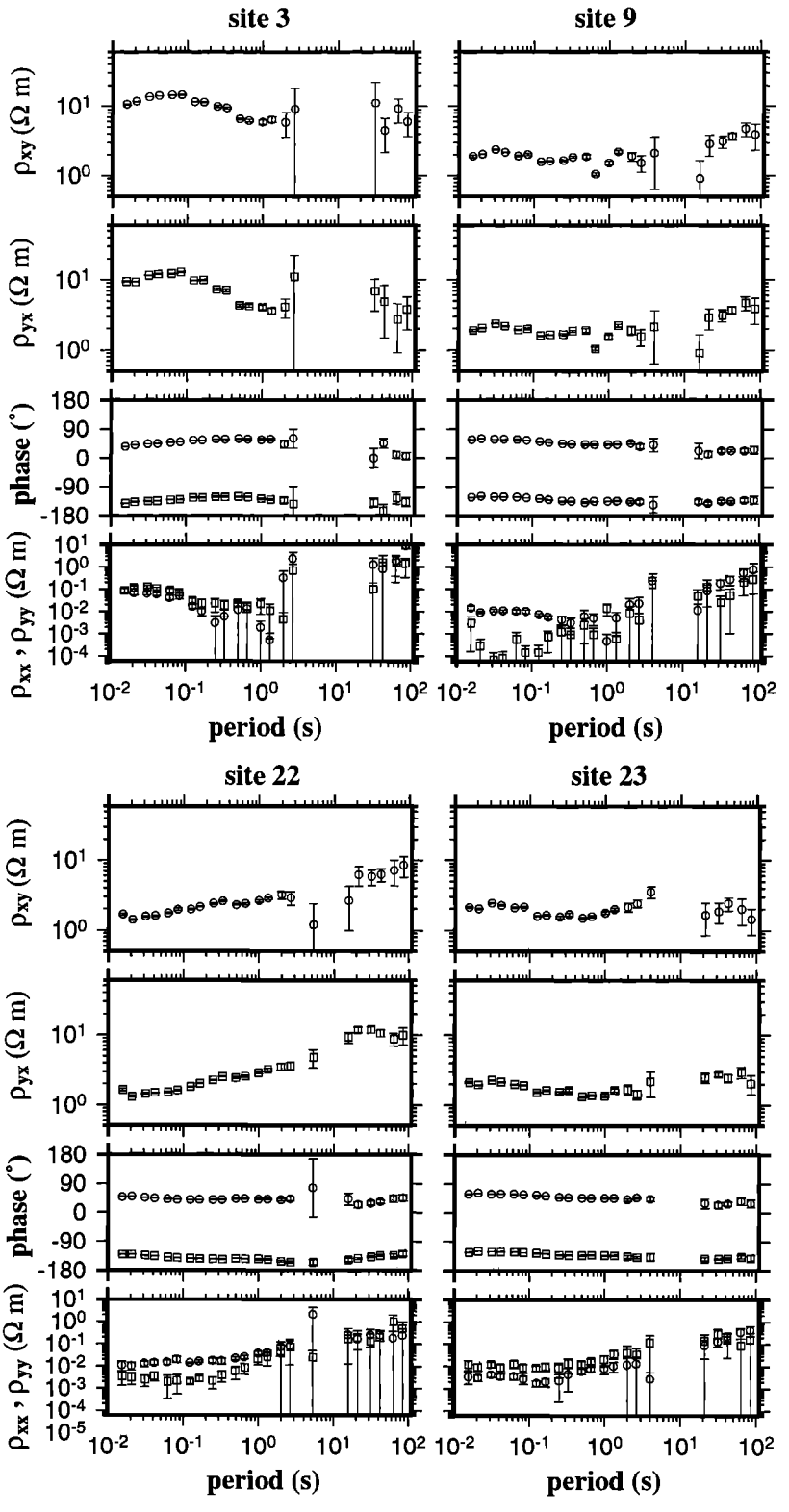

Figure 6. Example of magnetotelluric impedance at four sites (3, 9, 22, 23) (see text for details).

data points at most stations. Sometimes, the data at the longest periods exhibited nonphysical behavior such as abrupt changes of slope of the apparent resistivity and phase curves. In subsequent modeling (see below), we did not use all the available periods for numerical reasons. We selected a set of eight periods, 85.3, 42.7, 21.3,2.0, 0.67, 0.25, 0.0625, and 0.0208 s for which the impedance was reasonably well-determined at all sites.

Over a one-dimensional (1-D) medium, the tensor reduces to a single impedance, while in two-dimensional (2-D) situations and in the 2-D reference frame the impedance tensor Z is purely off-diagonal. In three-

dimensional (3-D) situations the impedance tensor has all four elements nonzero. However, when a regional trend dominates the geological structures, the tensor may be decomposed into an apparent regional 2-D tensor and a distortion matrix that accounts for the local 3-D geological features. Several decomposition techniques have been proposed in recent years [e.g., *Groom and Bahr,* 1992], which often assume that the local 3-D distortion is galvanic. Given the very conductive environment of the Baringo-Bogoria area, galvanic distortion may not dominate over the self-induction of locally deviated electric currents. A more general decomposition technique is therefore preferred. In the general case, reducing the impedance tensor to a purely off-diagonal tensor in order to recover a regional trend involves rotation angles of the field components in the complex plane. In addition, different rotation angles are needed for the electric field (E field) and the magnetic field (B field) [*La Torraca et al.,* 1986]. *Counil et al.* [1986] show that one rotation angle may be set real for either the E field or the B field, leading to a conjugate complex rotation angle of the B field or the E field, respectively. They also show that there exists a rotation angle of the E field or B field real axis that either maximizes or minimizes the impedance tensor. This angle defines a maximum E direction (MED) or a minimum B direction [*Counil et al.,* 1986]. In a 2-D geometry the MED corresponds to the strike of the 2-D structure or to the direction perpendicular to it, depending on the nature of the medium underneath. Ninety degree rotations of the MED may be observed over a short distance when two sites lie either side of a large resistivity contrast.

We applied this technique to calculate the MED and the maximum and minimum complex impedance values at each site and each period. The impedance is a minimum in the direction perpendicular to the MED. We report the mean MEDs for the shortest and the longest periods in a histogram (Figure 7). The MED would be weakly frequency-dependent and similar at all sites if a regional trend dominated the data. However, we do not observe a single dominant trend in the MEDs. Two directions dominate: N120°-140° at short periods and about N180°- 200° at long periods. Both directions are well-documented tectonic trends (Figures 1 and 3).

3.2.2. Data modeling. The complexity of the tectonic setting in the BBB as well as the observed variability in the MT impedance both with frequency and between sites suggest that 3-D modeling of the data is required. Recent progress in developing efficient electromagnetic and MT 3-D forward solutions has allowed a marked improvement in the modeling of MT data, otherwise interpreted using a 2-D approximation [e.g., *Mackie et al.,* 1996]. Solutions to 3-D inverse problems are still uncommon because of the numerical cost of solving the fully nonlinear induction problem and the limited number of situations where there are adequate data for 3-D modeling.

Although the adverse field conditions forced us to limit the survey to the BBB with consequently no stations on the edges of the area, we nevertheless consider that this data set is suited to 3-D inversion. The approach used is based on the minimization of the misfit between the data and model response, carried out with a nonlinear steepest gradient method [e.g., *Fisher and LeQuang,* 1981] selected on the basis of simplicity and robustness. A full 3-D forward calculation is needed at

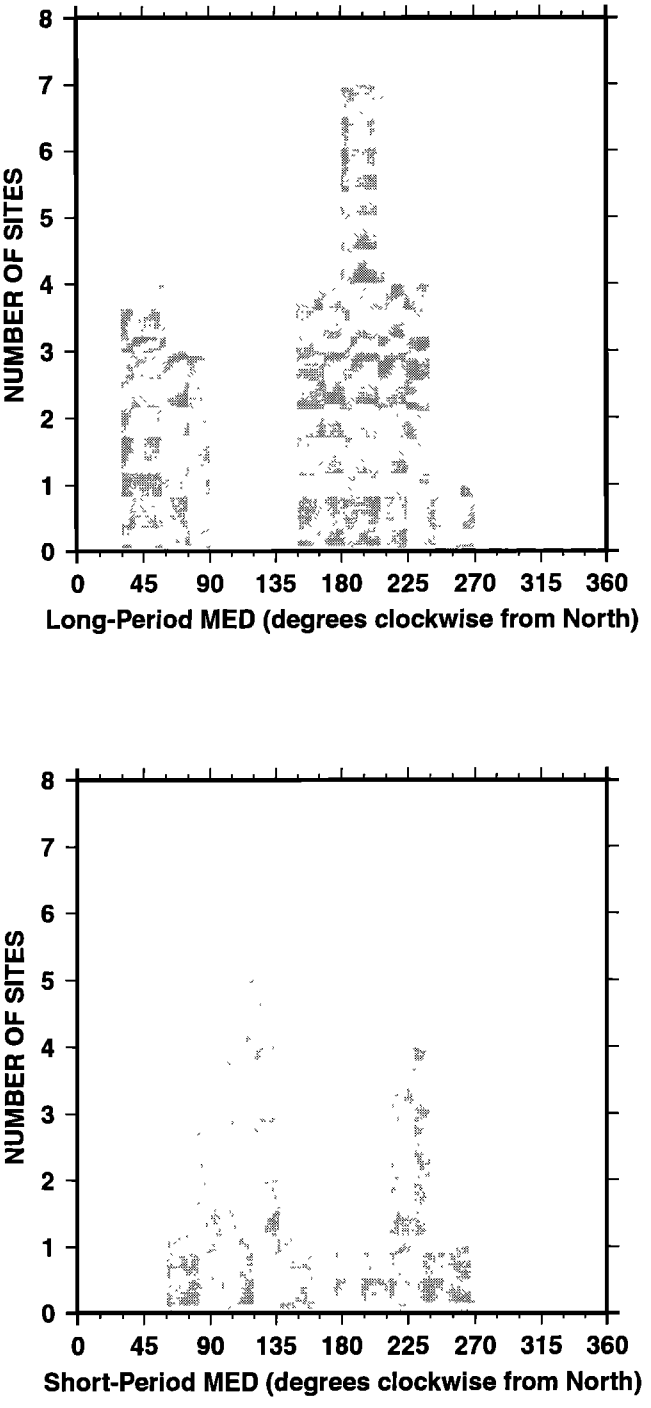

Figure 7. Histogram of the MED for (bottom) the mean short-period and (top) the mean long-period MT impedance (see text for details).

each iteration. This approach was used successfully in two dimensions on seafloor long-period MT data modeling [*Nolasco et al.*, 1998] and in three dimensions on VLF data [*Hautot et al.*, 1999].

Three-dimensional modeling of the data requires a careful preliminary parameterization of the region studied. We determined the large scale layout of the 3-D model with preliminary 2-D modeling of the MT data along an east-west profile (Figure 4). The results from the VES soundings were used to define the shallow structure of the 3-D model. The sensitivity of the data to the main features observed in the final model was tested. Finally, we considered the effect of the topography of the escarpments on the model.

3.2.2.1. Three-dimensional upper layers from the VES results: We generated four layers resistivity maps from the 1-D resistivity sections obtained at each VES site (Figure 4). We observed that the resistivity sections vary smoothly across the BBB, allowing interpolation onto a grid that was subsequently used to parameterize the shallow portion of the initial 3-D model. The maps are presented in Figure 8. Layer 1 is uniformly resistive except near Lakes Baringo and Bogoria. The resistivity increases smoothly from the SE to the NW in layers 2 and 3, which suggests a smooth transition of the infiltration from the alkaline Lake Bogoria to the freshwater Lake Baringo areas. The resistivity structure in the layer 4 is more complex than in the upper layers and seems to be controlled by structural features. Resistivity of the bottom two layers was allowed to vary during 3-D modeling, while the two top layers were kept constant throughout the analysis.

3.2.2.2. Initial 2-D and 3-D models: Analysis of the MEDs (Figure 7) showed that a single direction could not be defined for the whole period range available. Nevertheless, given that the longer-period data are controlled to some extent by the mean N-S trend of the rift, we used 2-D inversion of eight MT stations along an E-W profile (from west to east, sites 12, 11, 10, 9, 17, 20, 22, and 19; Figure 4) to define the

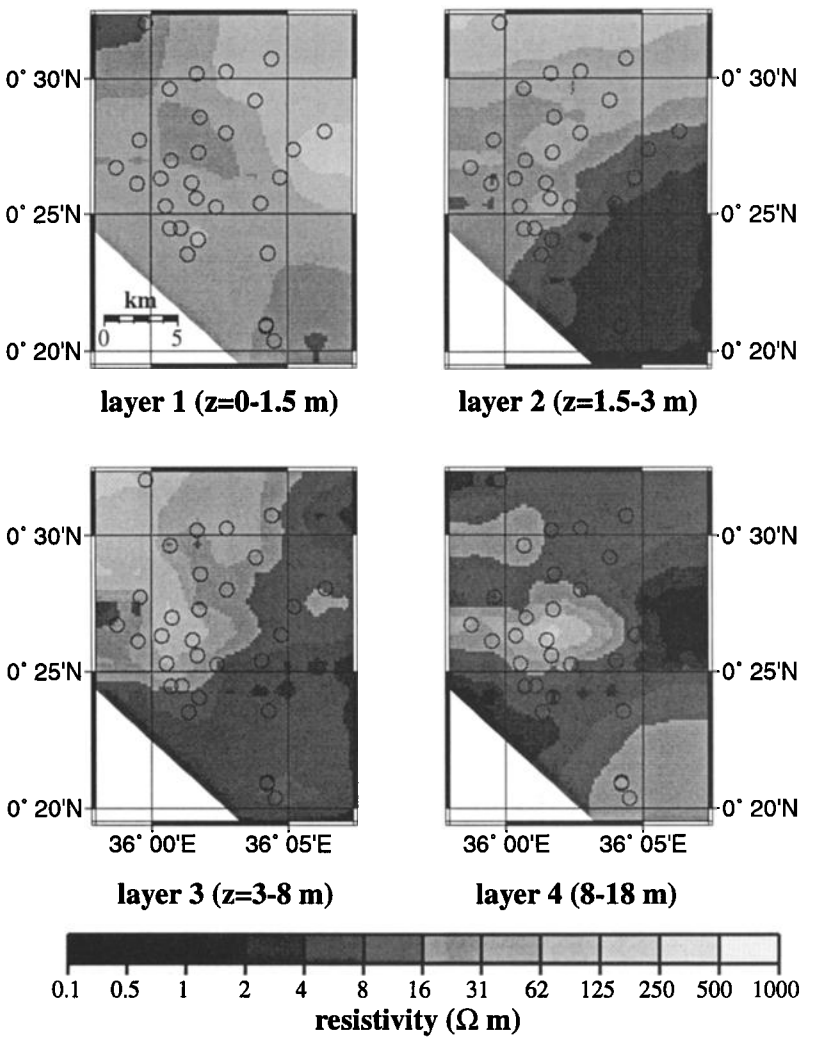

Figure 8. Electrical resistivity maps derived from the 1-D inversion of the vertical electrical soundings. In each layer the resistivity values obtained at each site are interpolated using the 3-D model grid.

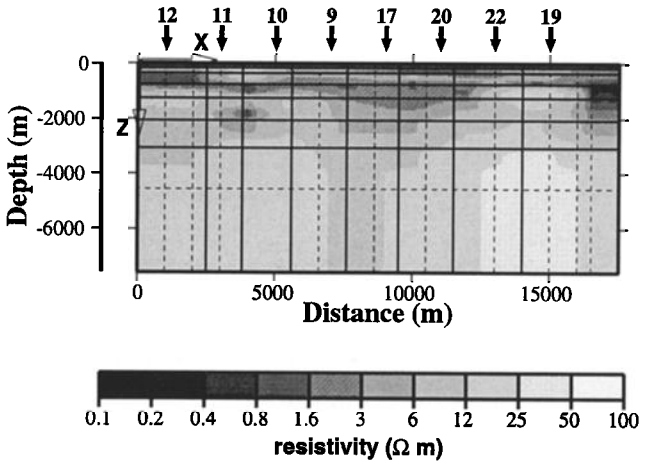

Figure 9a. Vertical grid used for 3-D modeling superimposed on the 2-D model obtained from the RRI analysis of the data along the profile depicted in Figure 4. The finer grid (dashed lines) is used for accurate calculation of the forward solution.

3-D starting model. We inverted both modes but only the off-diagonal terms of the impedance tensor using 2-D rapid relaxation inversion (RRI) [*Smith and Booker,* 1991], with the transverse electric (TE) mode set N-S and the transverse magnetic (TM) mode E-W. The model region is 16.5 km wide and 7.5 km high. The resulting resistivity cross section obtained is presented in Figure 9a. The top kilometer is very conductive on average (~3 Ω m) but with some resistive blocks (~20 Ω m). Below this, the subsurface is generally more resistive with appreciable lateral variations.

The 2-D model is used to initialize the 3-D modeling. The layout is composed of a central 3-D model of width equal to the width of the RRI 2-D model (Figure 9a), length 25.5 km and 8 km in the vertical direction (Figure 9b). The 3-D model volume is parameterized by 8 blocks in the x direction, 11 blocks in the y direction, and 12 layers in the z direction (the top four of which are from the VES resistivity model of Figure 8). The size of the blocks varies from 0.9 x 1.3 x 0.0015 km near the surface to 5 x 2. x 4.5 km at depth. Each block is homogeneous and is subdivided into a finer mesh to improve the numerical accuracy of the forward calculation (Figure 9b). The vertical grid is shown in Figure 9a. The resistivity in each cell is the average resistivity distribution in the surface defined by this cell in the RRI 2-D model. To the north and south of the 3-D block, the boundary condition is 2-D with a N-S strike. A 1-D resistivity section of width 17.5 km is added to the east and to the west of the central 3-D block to make a total width of 52.5 km, with resistivity that of the easternmost and westernmost cells of the 3-D block.

Following *Mackie et al.*'s [1993, 1994] suggestion of numerically filtering out the shorter-wavelength variations of the magnetic field by extending the model below the lower resistive crust, we added a 1-D electrical model for a continental rift with a layer of 500 Ω m from 8 to 15 km depth over a 10 Ω m half-space [*Rooney and Hutton,* 1977; *Jiracek et al.,* 1995]; this part of the model is not resolvable by our data.

3.2.3. Modeling. The discrepancy between the data and the 3-D model response is measured by the χ^2 misfit estimator:

$$\chi^2 = \sum \frac{(Z_m - Z_d)^2}{\sigma^2 w^2}. \quad (1)$$

Z_m is the response function of the model, Z_d is the datum, σ is the datum standard deviation, and w is a weighting factor. The weighting factor is equal to 2 (for a 95% confidence limit interval) except for a few data in the dead band and toward the longest periods where the transfer functions, in some instances, showed spurious behavior. For these data, w was increased to 3. The summation is over all selected frequencies at all sites. We added a regularizing factor R to the χ^2 misfit estimator, so that the objective function minimized was $\chi^2 + \lambda R(\sigma)$. The regularizing term R controls the resistivity contrast between blocks and is the sum over all blocks of the vertical and horizontal squared differences in the logarithm of the resistivity between two adjacent blocks, and λ is a damping parameter to ensure that λR is of order χ^2.

The forward problem was solved with the 3-D finite difference algorithm proposed by *Mackie et al.* [1994].

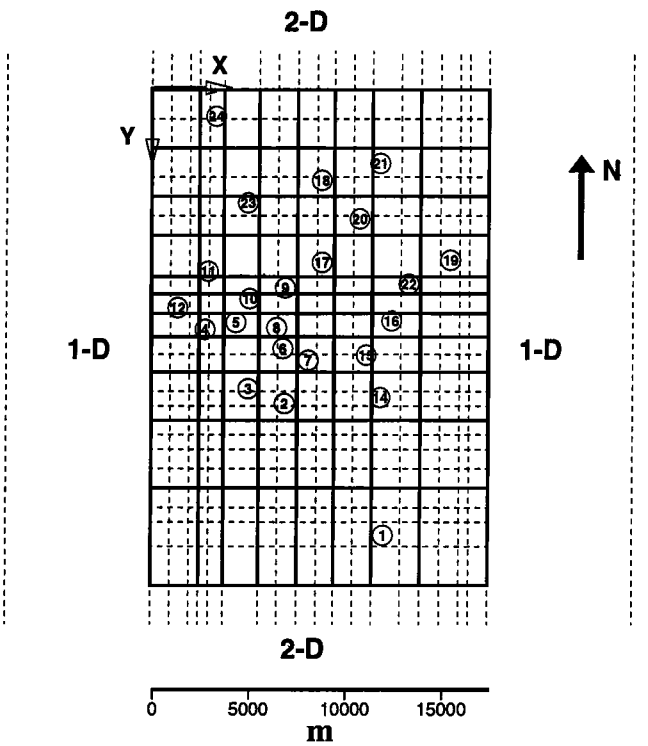

Figure 9b. Horizontal grid used for 3-D modeling. The open circles show the location of the MT sites considered for the 3-D inversion. The finer grid is used to calculate the forward solution. The 1-D structure is the vertical resistivity profile at the edges of the RRI 2-D structure.

The model parameters were the resistivity of the blocks in the 3-D part of the model from layers 3 to 12. The resistivities of layers 1 and 2, from the VES data, remained constant. The 1-D sections east and west of the 3-D central part were fixed during the minimization phase.

The calculation was carried out in several steps with two successive sets of data. First, we considered the full tensor at all 23 sites and for eight periods, 85.3, 42.7, 21.3, 2.0, 0.67, 0.25, 0.0625, and 0.0208 s (seven for sites 3, 4, 15, and 19), giving 1440 degrees of freedom. It proved to be difficult to adjust the small diagonal elements of the impedance tensor because of large signal to noise ratios at some stations. Hence once the misfit no longer changed, we continued the calculation with a new data set consisting of the two off-diagonal impedance coefficients (amplitude and phase) of the MT tensor in the MED reference frame at each site. The MEDs were not included in the minimization. The total number of degrees of freedom was then 720.

Once the misfit had reached a minimum, the 1-D resistivity values on the eastern and western sides of the 3-D central part as well as the thicknesses of the layers were adjusted by trial and error until no further reduction in the misfit was achieved. As a result, the total thickness of the 3-D part of the model, initially 8 km, was increased to 17 km. This moved the top of the conductive half-space that terminated the model to 20 km depth, in good agreement with the midcrustal conductor proposed by *Rooney and Hutton* [1977] south of the BBB. The final root-mean-square (rms) misfit, defined as

$$rms^0 = \sqrt{\frac{1}{N_s}\sum_{ls}\frac{\chi^2_{ls}(0)}{N_{95}(ls)}}, \qquad (2)$$

was 1.13. Here, N_s is the number of sites, the summation over ls is from 1 to N_s, N_{95} is the theoretical χ^2 misfit per site at the 95% confidence level, and (0) denotes this optimum model.

The agreement between the data and the model responses (the solid line) for selected sites (8-11, 14, 16, 17, 18, and 21) is shown in Figure 10a. The amplitude of the minimum and maximum impedance in the MED reference frame is scaled to apparent resistivity in ohm meters. The error bars are two standard deviations. Most of the model responses fit the data reasonably well, even at periods not included in the inversion. The observed and computed MEDs at sites 8-11, 14, 16, 17, 18, and 21 are shown in Figure 10b. Although the MEDs were also not included in the minimization procedure, the model retrieved them well at most sites. In some instances, however, the calculated MED was off by ~90° in a limited period band (sites 8 or 11) or aligned with the x or y axis (site 21). We observed that this happened when the maximum and the minimum amplitude of the impedance were quite close, a situation where the MED is not well defined.

A contour map of rms^0 at all sites for the initial and the final models is shown in Figure 11. The final misfit is distributed smoothly between all sites. The fit to the northwestern sites is in general better than that to the southeastern sites. The 3-D resistivity distribution in the final model is shown in Plate 1a for layers 3 to 8 and in Plate 1b for layers 9 to 11. The 12 layers of the initial model have been reduced to 11 because the original layers 10 and 11 were found to be virtually identical in the final model. Beneath layer 11, the medium is 1-D. The southwestern part of the model is masked because there are no data in this area.

In layers 3 and 4 (Plate 1a) the resistivity distribution has changed slightly compared to the initial VES resistivity model (Figure 8) and is well correlated to subsurface geology. We now recognize the contact between the Sandai alluvial fan and the IBF (Figure 4). Farther north, on the eastern side, the conductor is correlated with the Loiminang fan. Complex patterns appear in layers 5 to 9 (Plate 1a). Alternating conductive and resistive zones are observed with approximate directions either controlled by the N-S trend and its conjugate direction or by the N140° trend. The patterns change dramatically from layers 7 to 8 and from 8 to 9 (Plates 1a and 1b). Layer 10 is more homogeneous than the upper layers and is overall resistive. The resistivity distribution changes abruptly in layer 11 where the medium becomes much more conductive than in layer 10.

3.2.4. Sensitivity analysis. The model presented in Plate 1 reveals a variety of features at different scales and depths that may or may not be constrained by the data. It is necessary to investigate to what extent a given feature is actually required by the data. The model corresponds to a local (and probably not global) minimum of the misfit as a function of all model parameters. The resulting misfit is a compromise between misfits at all sites and at all frequencies, given (1) the 3-D parameterization of the BBB that we chose and (2) the data quality. Furthermore, the number of parameters sought in the modeling is of the order of the number of independent data (880 parameters from 1440 data). This implies that some parameters or sets of parameters are not resolved independently. We could have improved the ratio of the number of data to the number of parameters by using all periods available, but the numerical overhead would have been prohibitive.

With the restricted number of periods used, it is not numerically possible to prove that we have obtained a global misfit minimum or to calculate the resolution (i.e., the detailed topography of the misfit function) of all parameters. We had to restrict the sensitivity analysis to a set of key parameters, such as the thickness of each layer and the main geometrical features observed in the model, particularly at the greatest depths.

The procedure chosen is simple. We changed one parameter or one set of parameters, leaving all the others constant and calculated the corresponding change

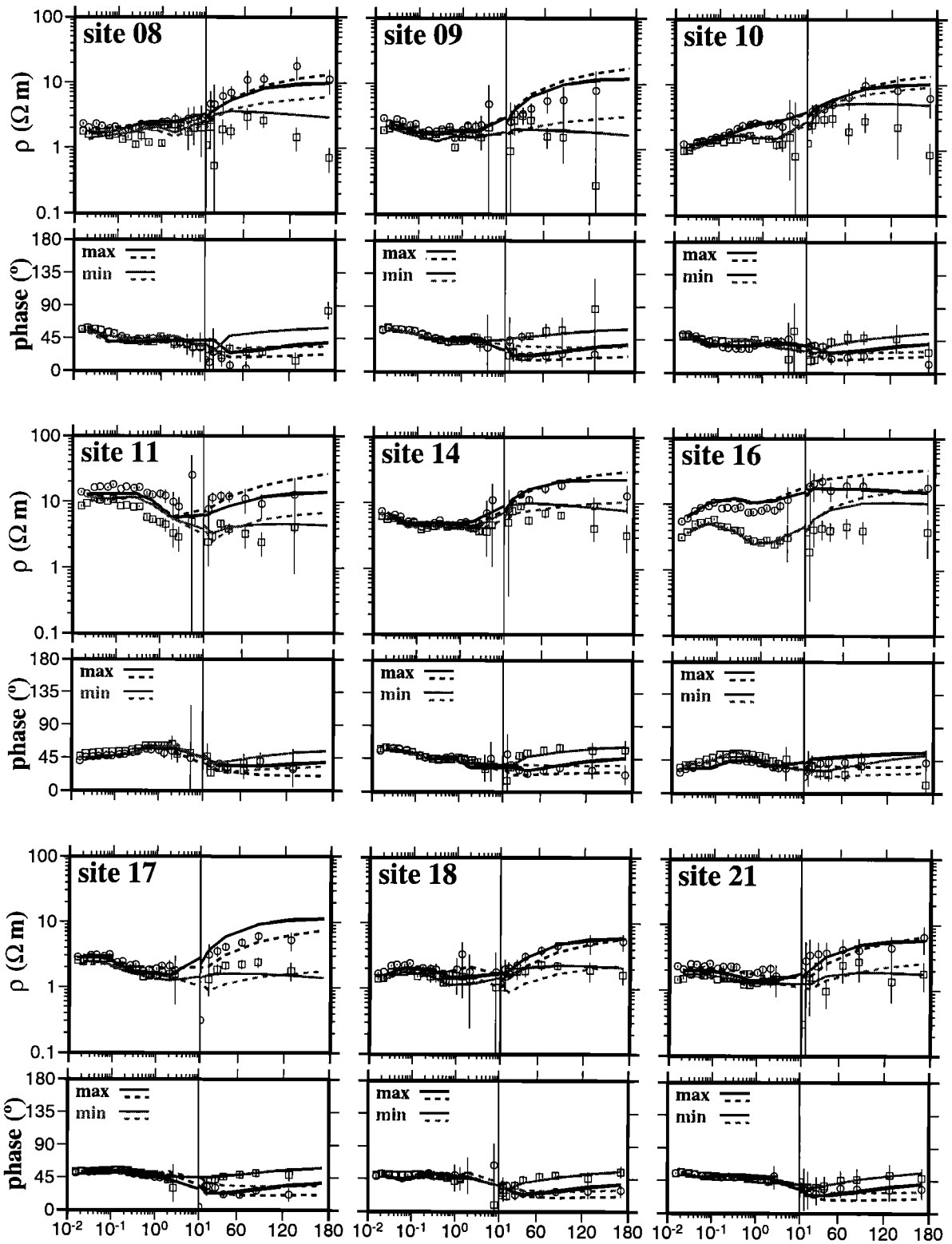

Figure 10a. Comparison between the observed (symbols) and computed (solid and dashed lines) maximum (circles) and minimum (squares) impedances in the MED reference frames at nine sites (8-11, 14, 16, 17, 18, and 21). The period (x axis) is on a logarithmic scale from 0.01 to 10 s and a linear scale from 10 to 180 s. The solid line is our preferred model response and the dashed line is for the new model, composed of layers 1-10 (Plates 1a and 1b) and a half-space of resistivity equal to 54 Ω m (see text for details).

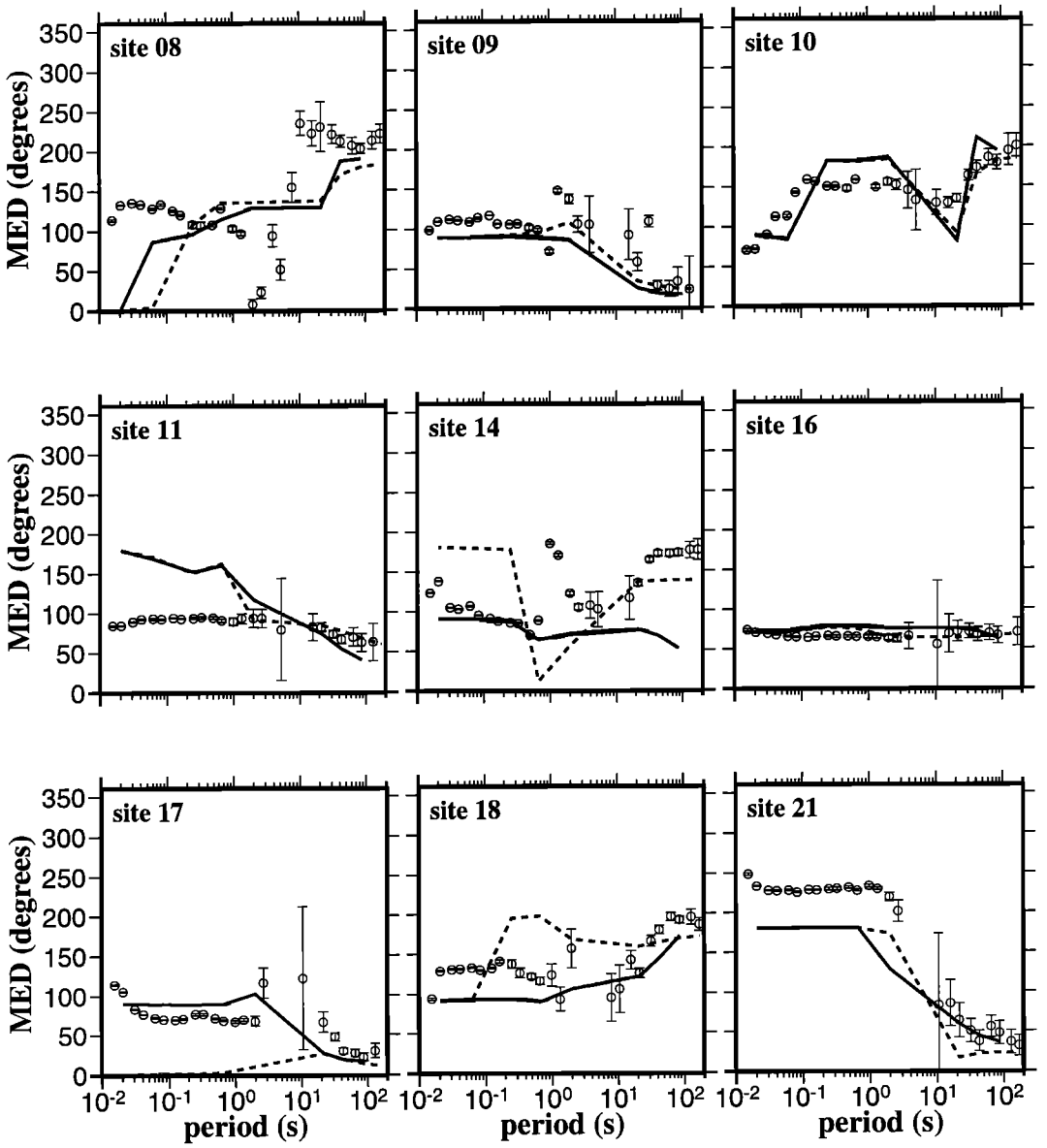

Figure 10b. As for Figure 10a for the MED at the nine selected sites.

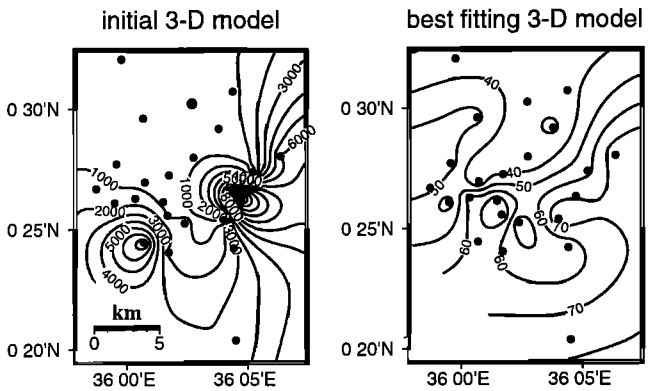

Figure 11. Contour plots of the misfit per site for the initial 3-D model (contour interval of 1000) and the best fitting model (contour interval of 10).

in misfit. We found as expected that although the final misfit is smooth over the BBB, its sensitivity to a change in the model parameters is quite variable from one site to another. Because of the geographical location and/or the data quality, the fit at a given station either may change significantly compared to other stations or may not change at all. The pattern is sometimes complicated: changing a model feature may decrease the misfit at some sites and increase it at others. In some instances, however, a change in a given parameter or a set of parameters may increase the misfit at all stations. In order to define a criterion to decide whether or not the misfit changed significantly so that the change in a parameter was no longer acceptable, we defined the following functions:

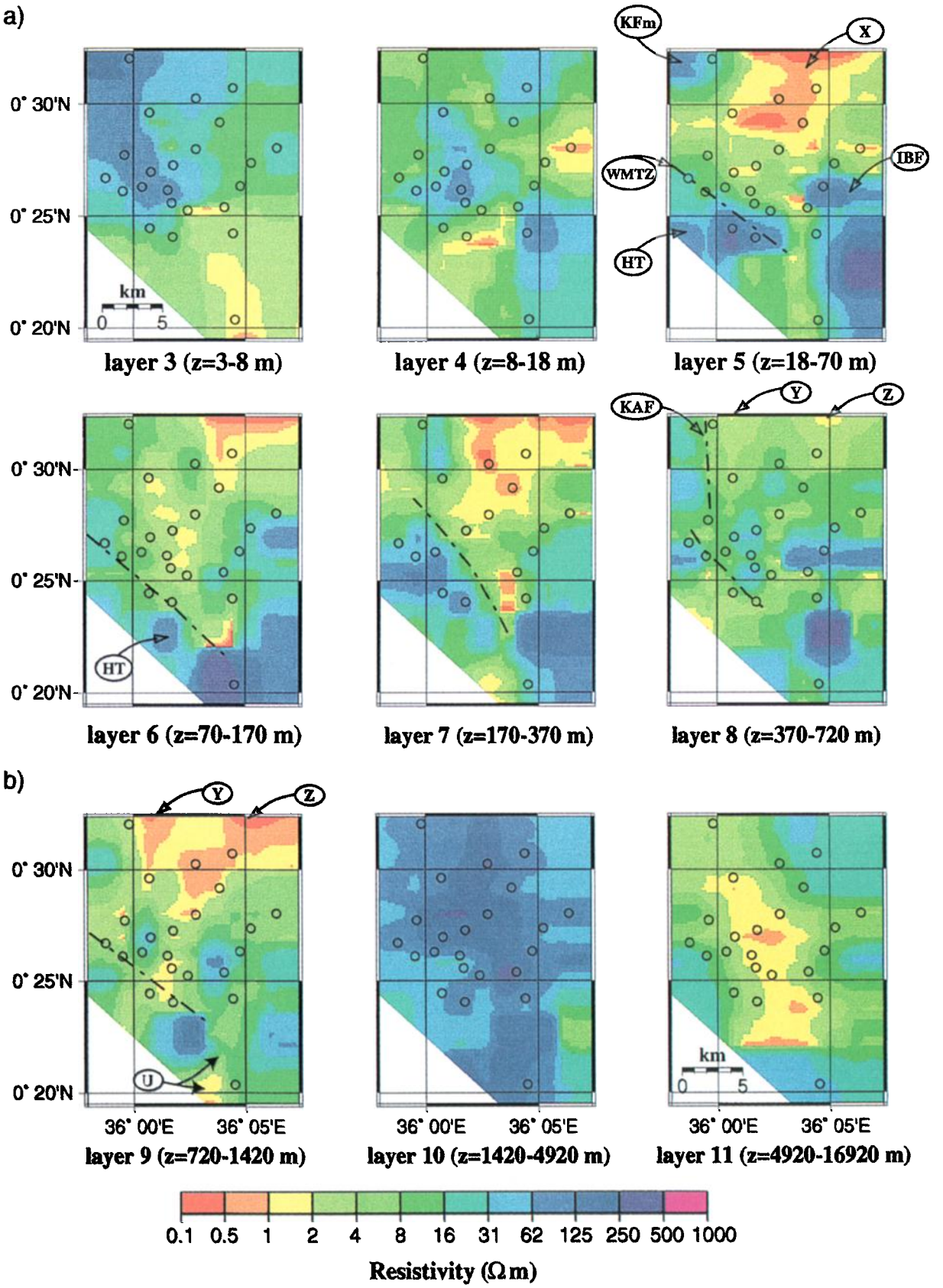

Plate 1a. Resistivity maps for layers 3-8 of the best fitting 3-D model. The southwestern part of the model has been masked because there are no MT sites in this area. The open circles are the MT sites. The main tectonic units are indicated by their keys and by heavy dashed lines. KFm, Kapthurin formation; WMTZ, Wasages- Marmanet Transverse Zone; HT, Hannington Trachyphonolites; IBF, Ilosowuani- Bechot Fault; KAF, Kapthurin Fault; U, W, X, Y, and Z, see text for details. **Plate 1b.** Same as Plate 1a, except for layers 9-11

$$(\Delta rms^m)^2 = \frac{1}{N_s}\sum_{ls}^{N_s}\frac{[\chi^2_{ls}(m)-\chi^2_{ls}(0)]}{N_{95}}, \quad (3a)$$

$$(\Delta rms^+)^2 = \frac{1}{N_s}\sum_{ls}^{N_{sp}}\frac{\{[\chi^2_{ls}(m)-\chi^2_{ls}(0)]\geq 0\}}{N_{95}}, \quad (3b)$$

$$(\Delta rms^-)^2 = \frac{1}{N_s}\sum_{ls}^{N_{sm}}\frac{\{[\chi^2_{ls}(0)-\chi^2_{ls}(m)]> 0\}}{N_{95}}, \quad (3c)$$

$$\varepsilon^+ = \Delta rms^+/rms^0,\ \varepsilon^- = \Delta rms^-/rms^0,$$
$$\varepsilon^m = \Delta rms^m/rms^0. \quad (4)$$

N_{sp} (N_{sm}) is the number of sites where the misfit increases (decreases) for a given change in a model parameter, ε^- measures the fractional decrease in misfit per site, relative to the total number of sites, while ε^+ measures the fractional increase in misfit per site, relative to the total number of sites. When $N_{sp} \cong N_s$, ε^m describes the total relative increase or decrease in misfit for all sites. We considered 0.1 (10%) for ε^m or ε^+ as the threshold above which the value of the parameter tested was not acceptable. This is an arbitrary limit in itself, so we simultaneously considered the amount the parameter changed to reach this threshold as well as the number of sites that contributed to this misfit increase. Furthermore, any value of ε^- was acceptable unless the number of sites implicated was too small. The tests presented hereafter obviously only provide a semiquantitative estimate of the sensitivity of the data to a given parameter or set or parameters but nevertheless are an indication of the robustness of our model.

3.2.4.1. Layer thicknesses and 1-D basement: The choice of the layering of the model was based on the preliminary 2-D data inversion (see above). The number of layers required by the data and the uncertainties in their thicknesses must be considered. We already mentioned that two distinct layers in the starting model, between 1420 and 4920 m, turned out to be similar in the modeling. Hence they were combined into a single layer, now layer 10 (Plate 1b), without a change in misfit. The sensitivity of the data to a given layer thickness was tested by varying the latter, keeping the rest of the model constant. Having set ε^m to 10%, the approximate range of acceptable thicknesses is 45 to 55 m for layer 5, 90 to 110 m for layer 6, 180 to 220 m for layer 7, 310 to 460 m for layer 8, and 630 to 770 m for layer 9. The relative uncertainty in layer thickness is therefore fairly small and ranges between about 10% and 20%. For these layer thickness variations the misfit increases at all stations.

The uncertainty in the thickness of layer 10 is larger than that of the upper layers probably because the data are limited toward the long periods and do not resolve the bottom of the layer well. For ε^m=10%, the thickness ranges from about 2.0 to 4.5 km. Nevertheless, this resistive layer is required by the data. A closer inspection of the misfit per site shows that they vary significantly over the area. For a thickness of 4.5 km, 16 sites see their misfit increase (ε^+=0.14) and 7 sites have a lower misfit than the original model (ε^-=0.08); for a thickness of 4 km, ε^+=0.12 for 11 sites and ε^-=0.11 for 12 sites; similarly, for a 2-km thickness, ε^+=0.16 for 10 sites and ε^-=0.12 for 13 sites. Hence the actual range of thicknesses could be less than previously indicated, 2.0 km to ~4.0 km.

Finally, the bottom of layer 11 (Plate 1b) and the 1-D model of the base of the crust and top of the mantle comprising a 3-km-thick homogeneous layer overlying a conductive half-space are not constrained by the data. The extent to which the conductivity structure of layer 11 is constrained is discussed in section 3.2.4.2.

In summary, the layering of the top first 1500 m is reasonably well constrained by the data. The presence of a resistive layer beneath is required and its thickness ranges from about 2 to 4 km. This layer seems to overlay a more conductive heterogeneous structure, the bottom of which is not resolved.

3.2.4.2. Resistivity structures: Testing the sensitivity of the data to the model resistivity distribution is complicated by the fact that it is numerically infeasible to test the resistivity in each cell. Instead, we focused on three main features whose resolvability by the data is questionable. We considered the sharp changes in resistivity from layer 7 to 8 and from layer 8 to 9. We also studied the sensitivity of the data to the structures observed in layers 5 to 7 (Plate 1a) on the southeastern edge of the area which has no sites directly above it but is bordered by several. Finally, we studied the robustness of the heterogeneous features observed in layers 10 and 11 (Plate 1b). The sensitivity of the data to the structure in layer 8 was tested by altering the resistivity distribution in this layer to an intermediate structure interpolated between layers 7 and 9. The value of ε^m increased to 141%, and the misfit at all sites increased dramatically. We thus concluded that the rapid resistivity changes at this depth are required.

In the zone extending from south of site 19 to the southern limit of the model from 18 to 370 m depth (layers 5 to 7, Plate 1a), the resistivity ranges from ~40 to ~500 Ω m. We multiplied the resistivity of the relevant blocks by a factor varying from 1/10 to 10. Acceptable values ($\varepsilon^m \leq$ 10%) are obtained only for factors of >0.5, i.e., the resistivities must be at least half their initial values, confirming that this resistive structure is required by the data at all sites.

The resistive layer 10 in Plate 1b shows an approximate N-S axis, away from which the resistivity decreases from ~150-250 Ω m to ~20-70 Ω m to the west and east. In order to test whether or not this heterogeneity is resolved, we ran three models in which we set the resistivity in this layer to a constant value, first 195 Ω m, second equal to the mean log(resistivity) in the layer (54 Ω m), and third, 20 Ω m. The values for ε^+ are 26%,

13%, and 23%, respectively (sites 16, 10, and 12 were affected); those for ε^- are 9%, 9%, and 10%, respectively (sites 7, 13, and 11 were affected). This indicates that a certain degree of heterogeneity seems necessary, but it is not possible to conclude definitively whether or not there is a resistive N-S axis. A mean value of 54 Ω m seems to be a reasonable compromise for this layer; a higher value does not seem to be acceptable.

An important feature revealed by the modeling is that layer 11 is conductive (Plate 1b). This part of the model is controlled by the data at the longest periods. For numerical reasons, the longest period used in the modeling was 85.3 s. The examination of the data (illustrated for nine sites in Figure 10a) shows that for periods ≤85.3 s, some sites do not show a clear decrease in the apparent resistivity or an increase in the phase (11, 16, 21). At several sites, however (8-10, 14, 17), where periods longer than 85.3 s are available, the data clearly suggest that there is a good conductor at depth.

Whether the conductive layer 11 (Plate 1b) is required by the data is first tested by replacing the layer and the underlying 1-D medium by a homogeneous half-space of resistivity equal to the mean resistivity of layer 10 (54 Ω m). This new model leads to an dramatic increase in misfit (ε^m=105%).

Then the model, composed of layers 1-10 (Plates 1a and 1b) and an underlying half-space of resistivity 54 Ω m, is used as the starting model for a new minimization in which the half- space resistivity is held fixed. The new model (not shown here) is very similar to the starting model. Some resistivity contrasts increased, but a slight change in the mean resistivity of the layers is observed (the maximum variation being for the layer 10, with a mean resistivity increasing from 54 to 61 Ω m). The response of this new model is shown in Figure 10a. As expected, only the response at the longest period is significantly modified compared to that of the preferred model (Plates 1a and 1b). A significant deterioration is observed at several sites (8, 9, 10, 11, 16, and 17). For the eight periods used in the modeling, the largest increases in misfit are obtained at sites 14, 17, and 18 over the conductive zone observed in layer 11 (Plate 1b), while misfit decreases are observed at sites 5, 8, 16, and 21 over the resistive part of layer 11 (Plate 1b). At periods longer than 85.3 s the misfit increases at most sites. This suggests that the heterogeneous structure observed in layer 11 (Plate 1b) is a feature resolved by the data.

In order to test further whether the conductive heterogeneity of the roughly N-S trend observed in layer 11 (Plate 1b) is a robust feature, the resistivity in the central area, ~1-4 Ω m, is increased to ~6-20 Ω m to the east and to the west. We first multiplied the resistivity values in the central area by a factor varying from 1/10 to 10. Within the limit of ε^m=10%, the multiplying factor is limited to a range 0.5-2.0, and therefore this zone must be conductive. Now we need to determine if the roughly E-W resistivity gradient is resolved. For this purpose, we set the resistivity of the layer to be homogeneous and equal to 1, 4, 7, 20, and 30 Ω m. None of these values leads to ε^+ less than 20%. This indicates that the hypothesis that layer 11 is homogeneous may be rejected. The misfit decreased at a maximum of 10 sites for a resistivity value equal to 7 Ω m, and ε^- was equal to 11%. All the sites are in the central and northern part of the layer, which is compatible with a roughly N-S conductor bordered to the east and to the west by less conductive material. The results at site 1 (at the southernmost part of the area) are inconclusive, and we cannot ascertain if the southern limit in layer 11 (Plate 1b) was resolved.

3.2.5. Topographic effect. The Marigat-Loboi Plain where we carried out the MT soundings has no notable variation in topography, with an average altitude of 1060 m. However, the plain is bordered by high faulted escarpments (~140 m) on its eastern and western sides and to the south by flexural topography affecting the Hannington lava flows (Figure 3). The MT fields at nearby sites are susceptible to distortion by this topography [*Ku et al.*, 1973], so we included a simplified model of it in the resistivity model obtained previously.

The misfit was slightly improved (ε^m=-3%). There is no notable difference between the responses of the model with and without topography, which is as expected given the very small change in misfit. Most of the improvement was observed at site 1. Clearly, the high conductivity of the Marigat-Loboi Plain filling limits the galvanic distortion associated with the topographic features, except very close to them.

4. Interpretation of the Resistivity Maps

The resistivity maps obtained for the shallow subsurface (Figure 8 and Plate 1a) can be interpreted from the surface geology (Figure 3), as well as by comparison with experimental modeling in similar geological contexts. The series involved in the central Kenya Rift correspond roughly to three main lithological groups, sediments, dominantly basic volcanism, and acidic basement rocks. The sediments are electrically very conductive (of the order of 1 Ω m). The volcanic series are, in general, resistive (a few hundred Ω m to 1000 Ω m or more) unless they are intensively fractured and the fractures filled with conductive material such as clays or hydrothermal deposits. Basement rocks are usually very resistive (>1000 Ω m) unless they too are fractured [e.g., *de Beer et al.*, 1975; *Losecke et al.*, 1988]. On this basis, the alternating conductive and resistive structures in the upper 1.5 km of the MT model may be correlated with sedimentary fill and volcanic formations. At greater depth the interpretation of the resistivity structure becomes more delicate and is discussed later on in section 5.

In the upper 18 m (layers 1 to 4) the resistivity distribution inferred from the modeling of the VES and the

high-frequency MT data (Figure 8 and Plate 1a) can be related to the Recent sedimentary cover of the Marigat-Loboi Plain that comprises the Loboi and Bogoria Silts, which have been estimated to be ~20 m thick, as well as the alluvial fan systems developed on both faulted margins of the plain [*Renaut,* 1982; *Tiercelin and Vincens,* 1987].

From 18 to 70 m depth (layer 5, Plate 1a) a conductive structure (labeled X) is bounded to the south and to the northwest by resistive features, which correlate with the main tectonic structures of the basin (Figure 3). To the southwest and northwest the resistive zone can be correlated with volcanic rocks belonging to the Hannington formation (HFm), and volcanic units associated with the fluvio-lacustrine KFm, respectively. To the southeast, the resistive structure seems to correspond to the volcanic rocks that form the IBF structure. The resistivity contrast observed along a N140° trend may be correlated with the contact between the recent sediments of the Marigat-Loboi Plain and the Hannington lavas and seems to correspond to the known position of the WMTZ on surface (layer 5, Plate 1a and Figure 3).

The conductive areas (layer 5, Plate 1a) clearly correlate with the present sedimentary basin. Two main axes of deposition can be defined.

1. A N-S axis, marked by a conductive feature several kilometers wide in the north of the area studied, clearly correlates with the downstream channels of the Molo and Perkerra Rivers and with the southern limit of the Lake Baringo sedimentary infill, bordered to the east and west by the distal parts of the Loiminang and Marigat alluvial fans (Figure 3). To the south this conductive anomaly is only a few kilometers wide and can be correlated with the morphostructural straight that links the northern end of Lake Bogoria to the Marigat-Loboi Plain, presently occupied by the distal part of the Sandai alluvial fan and the downstream course of the Sandai River.

2. An E-W axis correlates with lateral sedimentary fluxes from the western and eastern basin borders, linked to the Kapthurin, Ndau, and Perkerra Rivers to the west and to a possible ancient stream of the Sandai or Ol Arabel Rivers to the east.

From 70 to 370 m depth (layers 6 and 7, Plate 1a) the resistivity distribution is simpler than in the upper layers and is dominated by a conductive N-S axis. The E-W axes are only expressed on the basin borders. The western, eastern, and southern borders of the basin are always clearly defined by moderately resistive features, linked to the volcanic rocks (HFm and older flows) affected by the KAF and IBF, and the WMTZ. Between layers 6 and 7 (70-170 m and 170-370 m), the S-W resistivity structure correlated with the WMTZ shows a significant shift toward the northeast, compatible with the existence of a flexural structure. The western border corresponding to the KAF is less clearly defined in layer 7 and also reveals a lateral shift to the east. The width of the basin in layer 6 is similar to its value in the upper layers and appears to be well controlled by the N140° trend in layer 7.

Between 370 and 1420 m depth (layer 8, Plate 1a, and layer 9, Plate 1b) the resistivity distribution differs from the upper layers. The internal structure of the basin in layer 9 is dominated by two conductive, narrow structures oriented north and north-northeast (Y and Z on Plate 1b). In layer 8 these two structures are much narrower and are characterized by a higher resistivity. In layer 9 the extreme southern end of the area studied shows a narrow, globally N-S oriented, conductive structure (U, Plate 1a) similar to the structure in layer 7. To the west, the N-S trending border of the basin (volcanic rocks associated with the KAF) observed in layer 7 is present in layer 8 and becomes weaker in the underlying layer. The NW-SE trend of the WMTZ is still visible in layer 9 but less clearly than in the upper layers.

Below 1420 m (layer 10, Plate 1b) the resistivity is uniformly higher. This thick, resistive layer (2000 to 4000 m, see section 3.2.4.1) is an important feature of the model. Its structural interpretation is discussed in section 5.

Beneath layer 10, the medium becomes significantly more conductive (layer 11, Plate 1b). The conductor is in the center of the basin and seems to have a more or less N-S trend. The data have no resolution at greater depth.

5. Deep Structure of the Baringo-Bogoria Basin

From the interpretation of various seismic and gravity data the top of the Precambrian basement beneath Lake Baringo should occur at between 2 and 5 km depth [*Swain et al.,* 1981; *Maguire et al.,* 1994]. In the upper crust, seismic velocities of >6 km/s are consistent with granitic material [*KRISP Working Party,* 1991], which can be correlated with Precambrian basement (gneisses and amphibolites) outcropping in the Elgeyo Fault escarpment [*Sanders,* 1963; *Maguire et al.,* 1994]. Given that a high resistivity contrast can be expected between the sediments infilling the BBB and the Precambrian basement, the deep, electrically resistive layer (layer 10, Plate 1b) could be made up of either volcanic rocks or Precambrian metamorphic rocks.

The bottom of the sediments and volcanic series, at a depth of 1.5 km in our model, could therefore be the top of the Precambrian basement. If so, the deep conductive body in layer 11 is a surprising feature of our model. It is elongated roughly N-S and could reflect a deformation zone in the crystalline basement; its trend is compatible with the continental scale shearing of the Precambrian basement [*Smith and Mosley,* 1993]. Conductive zones have been associated with weak zones in metamorphic belts at crustal depths [*de Beer et al.,* 1982], but the origin of the material whose properties give rise to low

resistivity still remains uncertain. A few possibilities are high temperatures or conductive material such as graphite or saline water saturating fractures [*de Beer et al.,* 1975]. Electrical conductivity anomalies measured in the Baringo area and its surroundings have been interpreted as arising from melting but at depths of >10 km, in the upper mantle [*Rooney and Hutton,* 1977]. If we assume that the top of layer 10 is indeed the basement, then the conductive layer 11 is no more than 4 km into the basement (assuming a maximum acceptable thickness of 4 km for layer 10). Furthermore, the mean resistivity of layer 10 seems to be $<\sim 200\ \Omega$ m, according to the sensitivity analysis, a value markedly low for the Precambrian basement. This does not exclude the possibility of the presence of a dike swarm at 5-10 km depth, related to the dense intrusion proposed to explain the gravity highs observed along the rift valley [*Swain,* 1992]. A hot and highly mineralized dike intrusion zone is probably electrically conductive. This would be compatible with the requirement that the medium be conductive over at least 8 km (see section 3.2.4) beneath layer 10 but would not satisfactorily explain the succession between layers 10 and 11, which is at too shallow a depth (4 km or so).

It seems that without rejecting the possibility of the presence of deep intrabasement structures, we may also suggest an alternative hypothesis to explain at the same time the resistive layer 10 and the underlying deep conductive zone beneath: the resistive layer may be related to a thick layer of volcanic rocks underlain by sediments. This interpretation is postulated by analogy with the structural model proposed on the basis of industrial seismic reflection and gravity data by *Mugisha* [1994] and *Mugisha et al.* [1997] for the Kerio Basin located to the west of the Baringo region (Figure 1b), consisting of a deep (>6 km) half graben containing Paleogene deposits. We suggest a similar structure for the Baringo Basin, with initial synrift sedimentary infill represented by the upper part of the conductive layer at level 11 (below 3.5-4.5 km depth). In this model the layer is overlain at between 1.5 and 3.5 km depth by the resistive horizon that could be related to a thick pile of volcanic flows, possibly representing the lower to middle Miocene Samburu Basalts and Rumuruti Phonolites that reach a total thickness of 1750 m in the Laikipia and Saimo Fault escarpments (Figure 2). The low average resistivity of this layer (54 Ω m) could be due to the fracturing and thin conductive sediment series it is expected to contain. Thus this proto-Baringo Basin would be dated between Paleogene and lower Miocene time and should therefore be contemporary with the deep Kerio Basin to the west. The 2-D model derived from the seismic Kenya Rift International Seismic Project (KRISP) 90 cross-rift profile [*Maguire et al.,* 1994] shows a low-velocity structure beneath the Kerio Valley (5.6 km/s), at a depth of ~8.7 km, which can be correlated with the sedimentary basin. The absence of a such structure beneath Lake Baringo (at the latitude 0°38'N) suggests that the Baringo Basin must be restricted to the south of the POKTZ. An earthquake study [*Tongue et al.,* 1994] propose the existence, north of the POKTZ, of a dike system linked to a linear magmatic chamber at depth and feeding the Ol Kokwe and Karosi volcanoes (Figure 3).

By comparing this interpretation of the Baringo Basin with the interpretation provided by *Mugisha et al.* [1997] for the Kerio Basin (Figures 2 and 12), it appears that the 500- to 1000-m-thick middle Miocene Uasin Gishu-Tiim Phonolite Formations, which are the lateral equivalent of the Rumuruti Phonolites in the Elgeyo-Saimo region, have been correlated on the Kerio seismic lines with a <150-m-thick seismic sequence (MMV of *Mugisha et al.* [1997]). Such a difference in thickness of this widely spread phonolite formation suggests another interpretation: We propose that the top of the Paleogene series as defined by Mugisha et al. could represent the top of the middle Miocene Uasin Gishu-Tiim Formations (Figure 12). As a consequence, the 600-m-thick sedimentary and volcanic units (MS and MMV) correlated in *Mugisha et al.*'s [1997] model with the Tambach (MS) and Uasin Gishu (MMV) formations could be reinterpreted as a formation not known in outcrop, which may represent the lowest units of the Ngorora formation, including a possible 150-m-thick volcanic flow represented by Mugisha et al.'s MMV sequence. Such an interpretation, implying a much thicker (>800-m-thick) Ngorora Formation than previously advocated, is compatible with a sediment deposited within a time span of 4.5 Ma [*Hill,* 1999] in the axial part of a volcano-tectonically active basin [*Renaut et al.,* 1999].

The new lithostratigraphic succession proposed for the Baringo Basin and correlated to the Kerio series should be associated with a deep negative Bouguer anomaly, similar to the one observed over the Kerio Basin [e.g., *Swain et al.,* 1981]. However, the axis of the central Kenya Valley is characterized by marked gravity highs [*Swain,* 1992], while the BBB has a small (about -10 to -15 mGal) low [e.g., *Swain et al.,* 1981]. The current interpretation of the structure of the deep crust from the recent results of the KRISP 90 seismic profile combined with gravity data involves high-density structures as shallow as 10 km to the north of the BBB related to dike injection of material denser than the basement [*Swain,* 1992; *Maguire et al.,* 1994]. Similar structures have been proposed by *Swain* [1992] in the same area and along profiles crossing the rift to the south. It seems reasonable to assume that the high-density layer is also present beneath the Marigat-Loboi Plain. The MT data cannot resolve the structure beneath the top of layer 11 (Plate 1b), but they do require the medium be conductive at depth. A possible transition between the top of layer 11, interpreted as a Miocene sedimentary basin and a deeper intrusion area, is indiscernible in the MT data. The indirect evidence for such a structure is only provided by the anomalously small gravity low in the BBB.

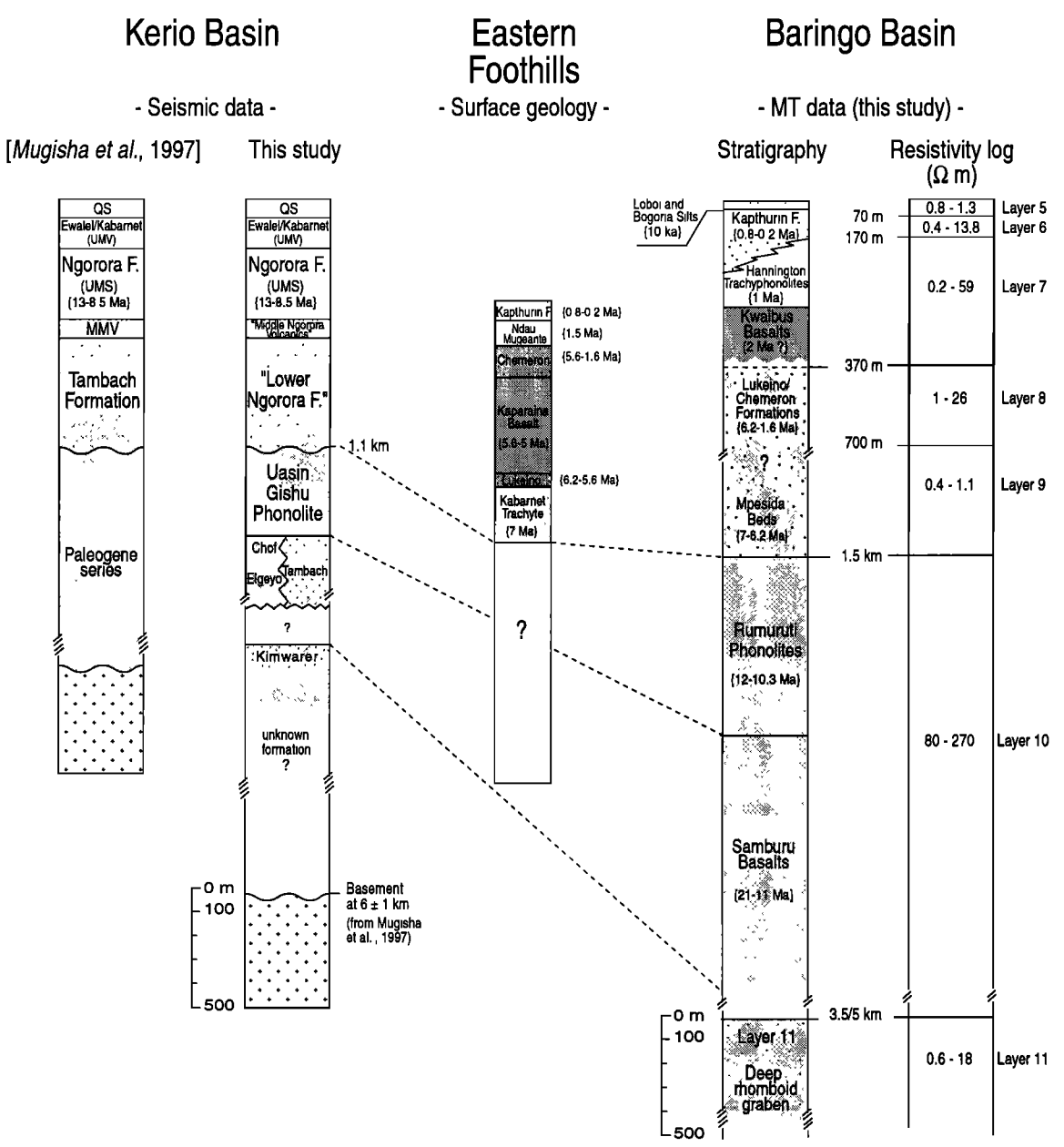

Figure 12. Interpreted stratigraphic series from the Kerio Basin to the Baringo Basin. From left to right, log proposed by *Mugisha et al.* [1997], log reinterpreted in this study, log of the Eastern Foothills, interpreted log for the Baringo Basin (this study), resistivity log deduced from the resistivity model (this study). The resistivity log was established from sites 17, 18, 20, 21, and 23 in the northern part of the model (Figure 4). We show the minimum and maximum resistivity in each layer in the area delimited by the five sites. Keys are given in the caption to Figure 2.

6. Structural Implications

The new lithostratigraphic succession applied here to the Baringo Basin leads us, first, to discuss and modify the structural interpretation proposed by *Mugisha et al.* [1997] for the adjoining Kerio Basin on the basis of industrial reflection seismic data and, second, to reconsider the rift model previously applied to the central Kenya system along the Elgeyo-Kerio-Saimo-Laikipia transect that implied a progressive easterly shift of both volcanic and tectonic activity from Miocene times onward [*Chapman et al.*, 1978; *Tiercelin and Vincens* 1987; *Morley et al.*, 1992].

6.1. Evolutionary Model for the Kerio-Baringo Rift Basins

Combining the known surface geology, reinterpreted seismic data (from the Kerio Basin), and newly acquired geophysical data set (BBB, this study) allows us to propose a new lithostratigraphic succession (Figure 13a) and evolutionary model (Figures 13b and 14) for the

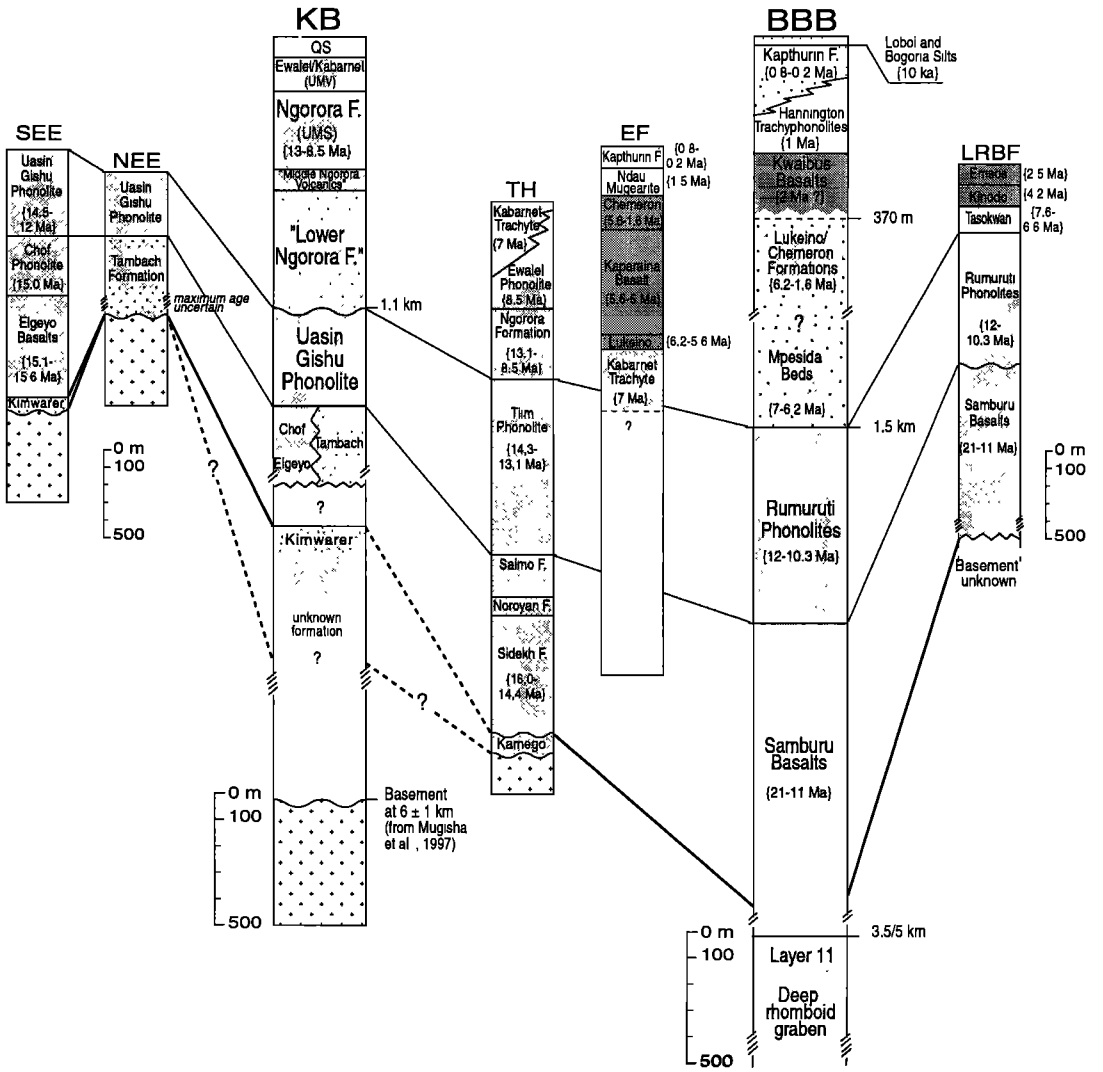

Figure 13a. Correlation between stratigraphic series from the Elgeyo Fault to the west to the Laikipia escarpment to the east. Baringo Axial Valley stratigraphic series are interpreted from the 3-D MT model. Note that we enlarged the reinterpreted Kerio log and the new Baringo log. Keys are given in the caption to Figure 2.

central Kenya Rift. The sections of Figure 13b illustrate five successive basinal templates from Paleogene times up to Present.

6.1.1. Stage 1, from Paleogene to lower Miocene. During this first phase of rifting, the deformation zone is located between a western rift boundary, the Kerio Fault (KeF) as defined by *Mugisha et al.* [1997], and an eastern boundary, the proto-Laikipia Rift Border Fault (LRBF) [*King,* 1978], which corresponds to a sparsely faulted flexure zone. Two, almost symmetrical, westward dipping half grabens develop progressively: the Kerio half graben to the west, bounded by the KeF, and the Baringo half graben to the east, bounded by a proto-Saimo Fault, separated by the Tugen Hills basement flexure zone. A similar scenario is known for the contemporary Lokichar basins in the northern Kenya Rift [*Morley et al.,* 1992]. These two Kerio and Baringo half grabens are filled by several kilometer-thick sediments. A small part of this infill can be represented by the conglomerates and sands of the Kimwarer and Kamego Formations. It is suggested that the upper part of this sedimentary infill is represented by the Tambach Formation, dated between 16 and 14 Ma. Contemporary volcanic activity occurs in the Elgeyo and Saimo regions with the eruption of the Elgeyo and Chof Formations to the west and the Sidekh Formation to the east (Figure 2). These volcanic series may form part of the infill of the deep Kerio half graben. In the Baringo half graben this stage is correlated with layer 11 (Plate 1b) of the resistivity model. No identifiable sedimentary formation in this area could represent part of this Paleogene-lower Miocene sedimentary infill. Volcanic activity in the Baringo-Laikipia region is represented during the lower-middle Miocene by the Samburu Basalts that form part of the Baringo Basin infill (Figure 13a).

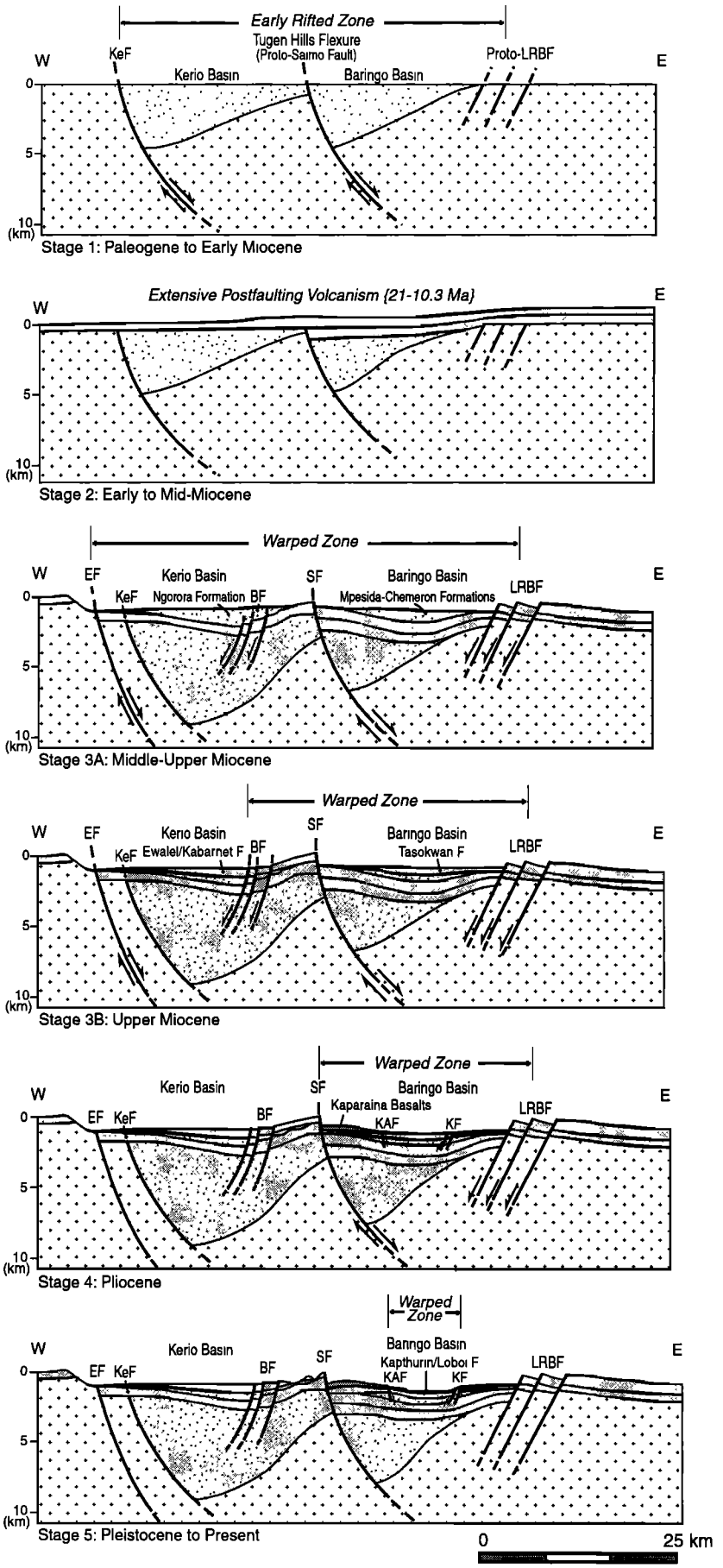

Figure 13b. Simplified diagram of the rifting evolution from Paleogene times to present. KF, Karau Fault; LRBF, Laikipia Rift Border Fault; EF, Elgeyo Fault; BF, Barwesa Fault; SF, Saimo Fault; KAF, Kapthurin Fault; KeF, Kerio Fault.

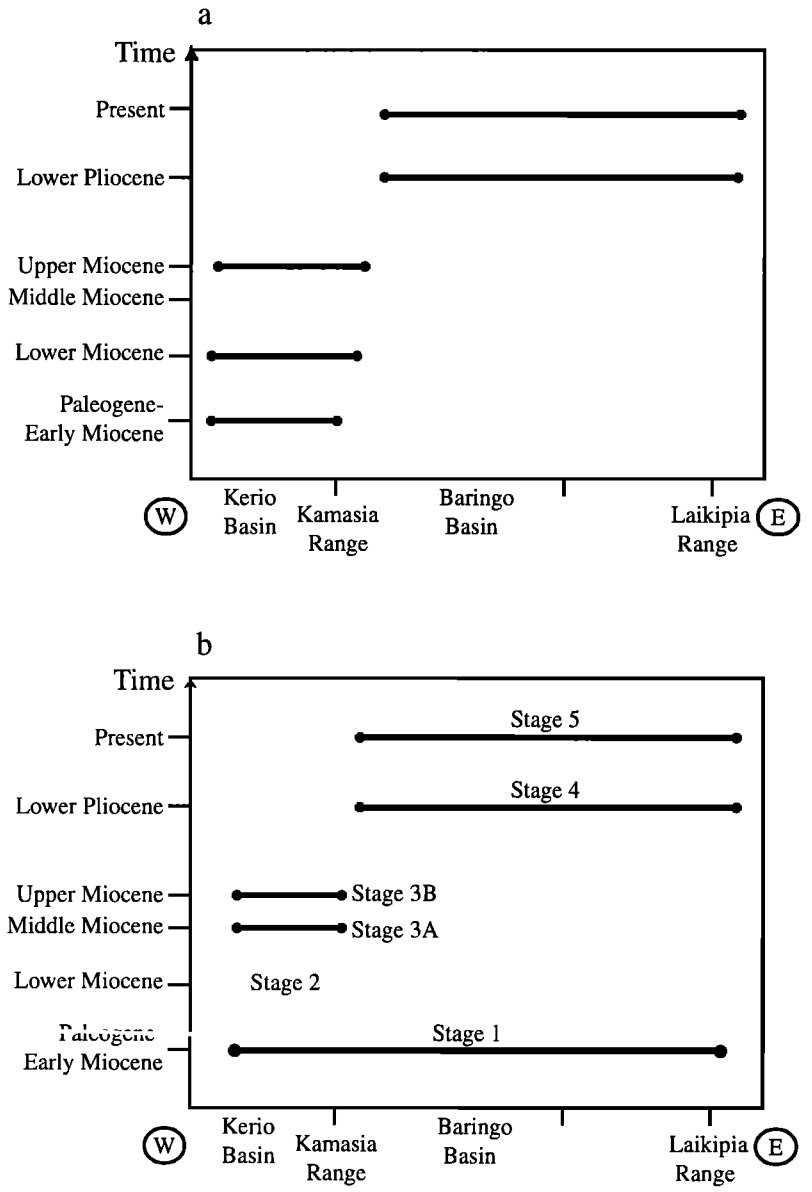

Figure 14. Time chart of tectonic activity in the central Kenya Rift. (a) From *Tiercelin* [1981], *Bosworth* [1985], *Morley* [1994], and *Mugisha et al.* [1997]. (b) Our proposed interpretation.

6.1.2. Stage 2, from lower to middle Miocene. The initial phase of rifting (Paleogene to lower Miocene) in central Kenya ends with a long period of intense volcanism, marked by the eruption of the 500- to >1000-m-thick Uasin Gishu, Tiim, and Rumuruti Phonolites that overflow both rift shoulders and cap the Kerio and Baringo Basins. In the Baringo Basin these formations are interpreted as corresponding to layer 10 of the resistivity model. In the Kerio Basin, it is proposed that this lava formation coincides with the top of the Paleogene series defined by *Mugisha et al.* [1997] (Figure 12).

6.1.3. Stages 3a and 3b (middle-upper Miocene). A second major phase of deformation affects the Kerio Basin. Considerable offset occurred along the western rift border, with the development of the Elgeyo Fault, and the erosion of the resulting Elgeyo escarpment contributes to the deposition in the Kerio Basin of the >800-m-thick fluvio and lacustrine Ngorora Formation. The extensive postfaulting volcanism resulted in the deposition on the western part of the rift of thick (330-700 m) upper Miocene lavas (Ewalel Phonolites and Kabarnet Trachytes) that cap the Nogorora Formation.

The eastern border of the rift is marked by a faulting episode that occurred before the eruption of the Tasokwan Trachytes (7.6-6.6 Ma), resulting in the submeridian structuring of the Laikipia complex N-S fault pattern that controls the distribution of the Tasokwan lava flows [*Griffiths*, 1977]. This observation suggests an interpretation of the two submeridian conductive features identified in layer 9 (Plate 1b) of the resistivity model as two N-S elongated grabens, formed parallel to the Laikipia fault escarpments during this tectonic episode and infilled by sediments. These sedimentary

basins could be contemporary with the upper part of the Ngorora Formation deposited to the west in the Kerio Basin or with the Mpesida Beds dated 7.2-6.7 Ma [*Hill,* 1999] (Figure 13a).

6.1.4. Stage 4 (Pliocene). The Pliocene period is marked by the concentration of volcanic activity and tectonic movement in the Baringo Basin to the east of the Tugen Hills. Between 5.4 and 3.9 Ma, fissure-style eruptions resulted in the deposition of the 600-m-thick Kaparaina Basalts on the hanging wall of the Saimo Fault [*Chapman and Brook,* 1978], followed by a major faulting episode that caused the deformation of the Kaparaina Basalts in close association with the development of the Lukeino/Chemeron sedimentary basins [*Chapman et al.,* 1978; *Hill,* 1999] (Figure 13a).

6.1.5. Stage 5 (Pleistocene to Present). The uppermost part of the resistivity model (layers 5, 6, and 7, Plate 1a) suggests that during this period the active axis of the rift is centered on the Baringo Basin, between the Saimo Fault and the easternmost Laikipia escarpment. The more resistive features visible in layers 5 to 7 of the resistivity model clearly correlate with the 150- to 300-m-thick Hannington Trachyphonolites and older lava flows (Kwaibus Basalts), which are affected by N-S trending faulted structures (KAF, IBF, and the Maji Moto grid fault zone) and by the N140° trending WMTZ. This could indicate that the N-S and N140° structural trends, having controlled the deposition of the initial rift sediments, still play an important role during the more recent stages of basin development.

The conductive, N-S trending axis (layer 7) can be interpreted as the main axial depocenter of the 125-m-thick fluvio-lacustrine KFm that accumulated above the Hannington lava flows. The E-W conductive axes could correspond to the drainage of the Saimo Fault escarpment to the west and Laikipia escarpment to the east, during the deposition of the KFm between 0.8 and 0.2 Ma.

6.2. Consequences in Terms of Rift Propagation

Defining the spatial distribution of the successive fault-controlled basins that developed since Paleogene times onward within the central Kenya rifted zone leads us to discuss and change markedly models of rift propagation previously applied to the Kenya Rift as a whole.

According to previous models, based mainly on surface geology, rifting is believed to have nucleated, as early as Paleogene time, on the western side of the present rift, in the Kerio area, while to the east, the first evidence of rift deformation was only expressed during the late Miocene by moderate flexuring along the Laikipia fault zone. During Pliocene to Recent time, rift deformation is assumed to have shifted eastward with respect to the Kerio Basin, focusing along the Baringo-Bogoria zone that belongs to the active axial trough of the Kenya Rift.

The recognition of a Paleogene deeply buried basin beneath the Baringo axial rift zone allows us to propose an alternative rift model that differs significantly from the concept outlined above, revealing a more complex organization of rifting at an early stage of the process (Figure 13b). One of the main assumptions of our model concerns the initial width of the rifted zone, which is here estimated to be 50-60 km, i.e., nearly twice that of previous models (stage 1, Figure 13b). The resulting Paleogene rift system may involve two similarly westerly tilted half grabens separated by an intervening basement high that can be interpreted as a proto-Tugen Hills.

During subsequent rifting stages the deformation seems to be largely distributed within the Kerio or Baringo Basin, but with no clear timing polarity. During mid-upper Miocene times (stage 3, Figure 13b), extension occurs principally within the western Kerio Basin, which is seen to maintain roughly the initial half-graben arrangement. To the east, the next stage of rift development starts later, during the lower Pliocene (stages 4 and 5, Figure 13b). In terms of rift migration, our model implies that the progressive widening of the rifted zone is accommodated by intrarift fault structures, possibly rejuvenating preexisting rift structures (e.g., Saimo Fault), rather than by fault networks propagating outward (to the east) through unstretched domains.

As indicated above, the initial geometry of the Baringo fault-controlled basin during the Paleogene rifting stage is unknown. However, the different maps of resistivity distribution (Plate 1) suggest strong control by both N-S (Kapthurin) and transverse faults (WMTZ) on the successive depocenters. This structural configuration is clearly documented for layers 5, 6, and 7 (Plate 1a). Therefore the Kerio and Baringo fault-controlled rift basins are likely to form synthetic half grabens bounded to the south by major N140° trending transverse fault zones. These are assumed to root at depth along large-scale basement discontinuities, and their geometrical relationships with the submeridian easterly dipping normal faults define an obtuse angle which is quite favorable for depocenter development, as has been shown for the Tanganika Rift (K. E. Lezzar et al., Control of normal fault interaction on the distribution of major Neogene sedimentary depocenters, Lake Tanganika, East African Rift, submitted to The Structure and Sequence Stratigraphy of Rift Systems, edited by J. R. Underhill, AAPG Memoir, 2000).

By now comparing the 3-D geometry of the Kerio and Baringo half grabens, as inferred from the available subsurface data sets, we observe marked differences. According to gravity data the Kerio half graben is assumed to occur as a 25-km-wide and 100-km-long structure [*Mugisha et al.,* 1997]. In contrast, there is no large Bouguer anomaly low associated with the Baringo half graben [e.g., *Swain et al.,* 1981]. From its present-day surface geology the southern part ap-

pears as a much smaller rhomb-shaped fault-controlled structure, ~25 km long (Figure 3). However, the initial length of the Baringo Paleogene-Miocene depositional area should have been much greater, as suggested by fault displacement-length scaling relationships generally accepted for fault populations [*Clark and Cox,* 1996; *Nicol et al.,* 1996]. Thus the 6 to 7-km-deep Baringo half graben corresponds to a nearly 100 to 120-km-long structure, i.e., quite similar to the adjoining Kerio Basin. Subsequent flexuring and fault segmentation of the Paleogene-Miocene half graben along transverse linear structures (Figure 3) accounts for the present-day lozenge-shaped geometry of the Baringo block.

Finally, it should be noted that this model for the central Kenya Rift, which implies (1) a relatively wide initial rift zone involving two similarly facing half grabens and (2) inward rift fault propagation, has also been proposed for the Lokichar-Lodwar half-graben system of the Turkana area farther north (Figure 1b) [*Morley et al.,* 1992]. Further subsurface geophysical investigations, such as the MT approach presented here, should be now carried out on the intervening Suguta rift valley (Figure 1a) in order to obtain a complete picture of the deep structure of the central/northern Kenya Rift as a whole.

7. Conclusions

We present the results from an interpretation of a magnetotelluric (MT) survey in the Bogoria-Baringo Basin in the central Kenya Rift. Three-dimensional modeling of the MT data is carried out using an iterative nonlinear minimization approach based on a 3-D forward calculation combined with a steepest gradient technique. The sensitivity of the data to the main features of the resulting model is tested. The electrical structure reveals alternating good conductors and resistive layers down to 4-5 km in depth. The resistivity distribution in the upper 1500 m is well correlated with recent geological events. From 1500 m to about 4 to 5 km, we obtain a thick resistive layer that we relate to the main mid-Miocene plateau-type flood phonolite. This layer overlies a conductive body, the top of which is interpreted as the sedimentary infill of a basin developed during the initial phase of rifting. It is suggested that the continuation downward of this conductive body is related to the intrusion of dikes. The recognition of a deeply buried Paleogene basin beneath the Baringo axial rift zone allows us to propose an alternative rift model that differs significantly from previous concepts, revealing a more complex organization of rifting at an early stage of the process.

Acknowledgments. This study has been realized as part of a cooperative program developed with the National Oil Corporation of Kenya (NOCK) within the framework of the 3D-3G Research Project supported by Elf Petroleum Norge AS (grant 2231-01 ELF to Tiercelin). Research authorization was provided by the Office of the President, Government of Kenya. We express our thanks to colleagues at NOCK for scientific, administrative and logistic support, especially J. K. Kwambai and F. M. Mbatau. Thanks are also expressed to William Kimosop from the Lake Bogoria National Reserve and to Elf Petroleum Norge AS for having authorized this publication. We are grateful to the UK Natural Environment Research Council Geophysical Equipment Pool for the loan of the MT equipment. We thank the reviewers, P. K. H. Maguire and R. L. Mackie, and associate editor, G. R. Jiracek, for their useful comments and suggestions.

References

Achauer, U., and the KRISP Teleseismic Working Group, New ideas on the Kenya Rift based on the inversion of the combined data set of the 1985 and 1989/90 seismic tomography experiments, *Tectonophysics, 236,* 305-329, 1994.

Andrews, P., and P. Banham (Eds.), *Late Cenozoic Environments and Hominid Evolution: A Tribute to The Late Bill Bishop,* Geol. Soc., London, 1999.

Baker, B. H., P. A. Mohr, and L. A. J. Williams, Geology of the eastern rift system of Africa, *Spec. Pap. Geol. Soc. Am., 136,* 67 pp., 1972.

Bishop, W. W., The late Cenozoic history of East Africa in relation to hominoid evolution, in *The Late Cenozoic Glacial Ages,* edited by K. K. Turekian, pp. 493-528, Yale Univ. Press, New Haven, Conn., 1971.

Bosworth, W., Geometry of propagating continental rifts, *Nature, 316,* 626-627, 1985.

Chapman, G.R., and M. Brook, Chronostratigraphy of the Baringo Basin, Kenya, in *Geological Background to Fossil Man,* edited by W. W. Bishop, pp. 207-223, Scot. Acad. Press, Edinburgh, 1978.

Chapman, G. R., S. J. Lippard, and J. E. Martyn, The stratigraphy and structure of the Kamasia Range, Kenya Rift Valley, *J. Geol. Soc. London, 135,* 265-281, 1978.

Chave, A. D., and D. J. Thomson, Some comments on magnetotelluric response function estimation, *J. Geophys. Res., 94,* 14,202-14,215, 1989.

Clark, R.M., and S. J. D. Cox, A modern regression approach to determining fault displacement-length scaling relationships, *J. Struct. Geol., 18,* 147-152, 1996.

Counil, J.-L., J.-L. Le Mouël, and M. Menvielle, Associate and conjugate direction concepts in magnetotellurics, *Ann. Geophys., 4,* 115-130, 1986.

de Beer, J.H., D. I. Gough, and J. S. V. van Zijl, An electrical conductivity anomaly and rifting in southern Africa, *Nature, 255,* 678-680, 1975.

de Beer, J.H., R. M. Huyssen, S. J. Joubert, and J. S. V van Zijl, Magnetometer array studies and deep Schlumberger soundings in Damara orogenic belt, south west Africa, *Geophys. J. R. Astron. Soc., 70,* 11-29, 1982.

Deino, A., L. Tauxe, M. Monaghan, and R. Drake, $^{40}Ar/^{39}Ar$ calibration of the litho- and palaeomagnetic stratigraphies of the Ngorora Fm., Kenya, *J. Geol., 98,* 567-587, 1990.

Dunkley, P. N., M. Smith, D. J. Allen, and W. G. Darling, The geothermal activity and geology of the northern sector of the Kenya Rift Valley, *Br. Geol. Surv. Res. Rep., SC/93/1,* 1993.

Fisher, G., and B. V. LeQuang, Topography and minimization of the standard deviation in one-dimensional magnetotelluric, *Geophys. J. R. Astron. Soc., 67,* 257-278, 1981.

Griffiths, P. S., The geology of the area around Lake Hannington and the Perkerra river, Rift Valley Province, Kenya, Ph.D. thesis, London Univ., London, 1977.

Griffiths, P. S., and I. L. Gibson, The geology and petrology of the Hannington trachyphonolite formation, Kenya Rift Valley, *Lithos, 13,* 43-53, 1980.

Grimaud, P., et al., Fault geometry and extension mechanisms in the central Kenya Rift, East Africa: A 3-D remote sensing approach, *Bull. Cent. Rech. Explor. Prod. Elf Aquitaine, 18,* 59-92, 1994.

Groom, R. W., and K. Bahr, Corrections for near surface effects: Decomposition of the magnetotelluric impedance tensor and scaling corrections for regional resistivities: A tutorial, *Surv. Geophys., 13,* 341-379, 1992.

Hautot, S., P. Tarits, and C. Tarits, Electromagnetic imaging of fissured crystalline bedrock in hydrogeology, in *Three-Dimensional Electromagnetics, Geophys. Dev. Ser.*, vol. 7, edited by M. Oristaglio and B. Spies, pp. 525-541, Soc. of Exp. Geophys., Tulsa, Okla., 1999.

Hay, D., R. F. Wendlandt, and G. R. Keller, Origin of Kenya Rift plateau-type flood phonolites: Integrated petrologic and geophysical constraints on the evolution of the crust and upper mantle beneath the Kenya Rift, *J. Geophys. Res., 100,* 10,549-10,557, 1995.

Hill, A., The Baringo Basin, Kenya: From Bill Bishop to BPRP, in *Late Cenozoic Environments and Hominid Evolution: A tribute to The Late Bill Bishop,* edited by P. Andrews and P. Banham, pp. 85-97, Geol. Soc., London, 1999.

Jiracek, G. R., V. Haak, and K. H. Olsen, Practical magnetotellurics in a continental rift environment, in *Continental Rifts: Structure, Evolution, Tectonics,* edited by K. H. Olsen, pp. 103-129, Elsevier Sci., New York, 1995.

King, B. C., Structural and volcanic evolution of the Gregory Rift Valley, in *Geological Background to Fossil Man,* edited by W. W. Bishop, pp. 29-54, Scot. Acad. Press, Edinburgh, 1978.

KRISP Working Party, Large-scale variation in lithospheric structure along and across the Kenya Rift, *Nature, 354,* 223-227, 1991.

Ku, C. C., M. S. Hsieh, and S. H. Lim, The topographic effect in electromagnetic fields, *Can. J. Earth Sci., 10,* 645-656, 1973.

La Torraca, G. A., T. R. Madden, and J. Koringa, An analysis of the magnetotelluric impedance for three-dimensional conductivity structures, *Geophysics, 51,* 1819-1829, 1986.

Le Gall, B., C. Le Turdu , J.-P. Richert, J.-J. Tiercelin, P. Gente, P. Sturchio, and D. Stead, A morphotectonic study of an extensional fault zone in a magma-rich rift type : the Baringo Trachyte Fault System, central Kenya Rift, *Tectonophysics, 320,* 87-106, 2000.

Le Turdu, C., Modèles tectono-sédimentaires 3-D des bassins en extension: Exemples du Rift du Kenya (Baringo-Bogoria et Magadi), du Rift Ethiopien (Ziway-Shala) et du Fossé Nord-Tanganyika, thèse, 416 pp., Univ. de Bretagne Occidentale, Brest, France, 1998.

Le Turdu, C., C. Coussement, J.-J. Tiercelin, R. W. Renaut, J. Rolet, J.-P. Richert, J.-P. Xavier, and D. Coquelet, Rift basin structure and depositional patterns interpreted using a 3-D remote sensing approach: The Baringo-Bogoria Basins, central Kenya Rift, East Africa, *Bull. Cent. Rech. Explor. Prod. Elf Aquitaine, 19,* 1-37, 1995.

Lippard, S. J., The stratigraphy and structure of the Elgeyo Escarpment, southern Kamasia Hills and adjoining regions, Rift Valley Province, Kenya, Ph.D. thesis, Univ. of London, London, 1972.

Losecke, W., K. Knödel, and W. Müller, Magnetotelluric survey in the northern Zambesi valley of Zimbabwe, *Rep. Proj. 84.2171.1,* Bundesanstalt für Geowiss. und Rohstoffe, Hannover, Germany, 1988.

Mackie, R. L., T. R. Madden, and P. E. Wannamaker, Three-dimensional magnetotelluric modeling using difference equations-Theory and comparisons to integral equation solutions, *Geophysics, 58,* 215-226, 1993.

Mackie, R. L., J. T. Smith, and T. R. Madden, Three-dimensional electromagnetic modeling using finite difference equations: The magnetotelluric example, *Radio Sci., 29,* 923-935, 1994.

Mackie, R. L., T. R. Madden, and S. K. Park, A three-dimensional magnetotelluric investigation of the California Basin and Range, *J. Geophys. Res., 101,* 16,221-16,239, 1996.

Maguire, P. K. H., C. J. Swain, R. Masotti, and M. A. Khan, A crustal and uppermost mantle cross sectional model of the Kenya Rift from seismic and gravity data, *Tectonophysics, 236,* 217-249, 1994.

McConnell, R. B., Geological development of the rift system of eastern Africa, *Geol. Soc. Am. Bull., 83,* 2549-2572, 1972.

Morley, C. K., Interaction of deep and shallow processes in the evolution of the Kenya Rift, *Tectonophysics, 236,* 81-91, 1994.

Morley, C. K., W. A. Wescott, D. M. Stone, R. M. Harper, S. T. Wigger, and F. M. Karanja, Tectonic evolution of northern Kenya Rift, *J. Geol. Soc., 149,* 333-348, 1992.

Mugisha, F., Processing and interpretation of seismic and gravity data from the Kerio and northern Malawi Rifts, Africa, Masters thesis, 161 pp., Univ. of Leeds, Leeds, England, 1994.

Mugisha, F., C. J. Ebinger, M. Strecker, and D. Pope, Two-stage rifting in the Kenya Rift: Implications for half-graben models, *Tectonophysics, 278,* 61-81, 1997.

Nicol, A., J. Watterson, J.J. Walsh, and C. Childs, The shapes, major axis orientation and displacement patterns of fault surface, *J. Struct. Geol., 18,* 235-248, 1996.

Nolasco, R., P. Tarits, J. H. Filloux, and A. D. Chave, Magnetotelluric imaging of the Tahiti hot spot, *J. Geophys. Res., 103,* 30,287-30,309, 1998.

Pickford, M. H. L., Late Miocene sediments and fossils from the northern Kenya Rift Valley, *Nature, 256,* 279-284, 1975.

Renaut, R. W., Late Quaternary geology of the Lake Bogoria fault-trough, Kenya Rift Valley, Ph.D. thesis, 489 pp., Univ. London, London, 1982.

Renaut, R.W., J. Ego, J.-J. Tiercelin, C. Le Turdu, and B. Owen, Saline, alkaline palaeolakes of the Tugen Hills-Kerio Valley region, Kenya Rift valley, in *Late Cenozoic Environments and Hominid Evolution: A Tribute to The Late Bill Bishop*, edited by P. Andrews and P. Banham, pp. 41-58, Geol. Soc., London, 1999.

Richert, J. P., J.-J. Tiercelin, and G. Vidal, Relief et structure, in *Le Demi-Graben de Baringo-Bogoria, Rift Gregory, Kenya, 30000 ans d'Histoire Hydrogéologique et Sédimentaire*, edited by J.-J Tiercelin and A. Vincens, *Bull. Cent. Rech. Explor. Prod. Elf Aquitaine, 11,* 256-281, 1987.

Ritter, 0., A. Junge, and G. J. K. Dawes, New equipment and processing for magnetotelluric remote reference observations, *Geophys. J. Int., 132,* 535-548., 1998.

Rooney, D., and V. R. S. Hutton, A magnetotelluric and magnetovariational study of the Gregory Rift Valley, Kenya, *Geophys. J. R. Astron. Soc., 51,* 91-119, 1977.

Sanders, L.D., Geology of the Eldoret area, *Rep. 64*, Geol. Surv. Kenya, 1963.

Smith, J. T., and J. R. Booker, Rapid inversion of two- and three-dimensional magnetotelluric data, *J. Geophys. Res., 96,* 3905-3922, 1991.

Smith, M., and P. Mosley, Crustal heterogeneity and basement influence on the development of the Kenya Rift, East Africa, *Tectonics, 12,* 591-606, 1993.

Swain, C. J., The Kenya Rift axial gravity high: A reinterpretation, *Tectonophysics, 204,* 41-52, 1992.

Swain, C. J., M. A. Khan, T. J. Wilton, P. H. K. Maguire, and D. H. Griffiths, Seismic and gravity surveys in the Lake Baringo-Tugen Hills area, Kenya Rift Valley, *J. Geol. Soc. London, 138,* 93-102, 1981.

Swain, C. J., P. K. H. Maguire, and M. A. Khan, Geophysical experiments and models of the Kenya Rift before 1989, *Tectonophysics, 236,* 23-32, 1994.

Tiercelin, J.-J., Rifts continentaux, tectonique, climats, sédiments. Exemples de la sédimentation dans le Nord du Rift Gregory (Kenya) et dans le Rift de l'Afar (Ethiopie) depuis le Miocène, thèse Doct. Etat Sci., 260 pp., Univ. de Aix-Marseille II, Aix en Provence, France, 1981.

Tiercelin, J.-J., and A. Vincens (Eds.), The Baringo-Bogoria half-graben, Gregory Rift, Kenya, 30,000 years of hydrological and sedimentary history, *Bull. Cent. Rech. Explor. Prod. Elf Aquitaine, 11,* 249-540, 1987.

Tiercelin, J.-J., J. Le Fournier, J.-P. Herbin, and J.-P. Richert, Continental rifts: modern sedimentation, tectonic and volcanic control: Example from the Bogoria-Baringo graben, Gregory Rift, Kenya, in *Geodynamic Evolution of the Afro-Arabic Rift System,* pp. 143-164, Accad. Naz. dei Lincei, Rome, 1980.

Tiercelin, J.-J., R. W. Renaut, G. Delibrias, J. Le Fournier, and S. Bieda, Late Pleistocene end Holocene lake levels in the Lake Bogoria basin, northern Kenya Rift Valley, *Palaeoecol. Africa, 13,* 105-120, 1981.

Tongue, J., P. Maguire, and P. Burton, An earthquake study in the Lake Baringo basin of the central Kenya Rift, *Tectonophysics, 236,* 151-164, 1994.

Williams, L. A. J., and G. R. Chapman, Relationships between major structures, salic volcanism and sedimentation in the Kenya Rift from the equator northwards to lake Turkana, in *Sedimentation in African Rifts,* edited by L. E. Frostick, R.W. Renaut, I. Reid, and J.J. Tiercelin, *Geol. Soc. Spec. Publ., 25,* 59-64, 1986.

S. Hautot, B. Le Gall, C. Le Turdu, P. Tarits, and J.-J. Tiercelin, UMR CNRS 6538 "Domaines Océaniques", IUEM/UBO, Place Nicolas Copernic, 29280 Plouzané, France. (hautot@sdt.univ-brest.fr; blegall@univ-brest.fr; tarits@sdt.univ-brest.f; tiercelin@univ-brest.fr)

K. Whaler, Grant Institute, Department of Geology and Geophysics, University of Edinburgh, West Mains road, Edinburgh EH9 3JW, Scotland, UK. (whaler@mail.glg.ed.ac.uk)

(Received August 25, 1999; revised May 31, 2000; accepted June 8, 2000.)